Title
High-throughput Synthesis and Metrology of Graphene Materials

Author
Ghazinejad, Maziar Ghazinejad

Publication Date
2012

UNIVERSITY OF CALIFORNIA
RIVERSIDE

High-throughput Synthesis and Metrology of Graphene Materials

A Dissertation submitted in partial satisfaction
of the requirements for the degree of

Doctor of Philosophy

in

Mechanical Engineering

by

Maziar Ghazinejad

September 2012

Dissertation Committee:

Professor Cengiz Sinan Ozkan, Chairperson
Professor Kambiz Vafai
Professor Mihrimah Ozkan

The Dissertation of Maziar Ghazinejad is approved:

Committee Chairperson

University of California, Riverside

Acknowledgment

I would like to express my sincere gratitude to my advisor Prof. Cengiz Ozkan, at University of California-Riverside for his support of my Ph.D. research, and his patience throughout my graduate studies.

My deep appreciations go to Prof. Mihri Ozkan in Department of Electrical Engineering of University of California-Riverside for her continuous scientific and moral support. I am grateful to Prof. Kambiz Vafai in Mechanical Engineering Department and Prof. Valentine Vullev in Bioengineering Department of University of California-Riverside for their scientific contributions, stimulating discussions, and supports.

I would like to acknowledge National Science Foundation, the UMass Materials Research Science and Engineering Center on Polymers (NSF-MRSEC), American Public Power Association (APPA-DEED), FCRP Center on Functional Engineered Nano Architectonics (FENA-SRC), and Graduate Division of University of California-Riverside for supporting my Ph.D. studies.

My love and appreciation go to my family, my mother Farangis Ghaziani, my father Esfandiar Ghazianejad, and my brother Mazdak, whom without their continuous care and supports I would not be able to complete my education. Maziar

ABSTRACT OF THE DISSERTATION

High-throughput Synthesis and Metrology of Graphene Materials

by

Maziar Ghazinejad

Doctor of Philosophy, Graduate Program in Mechanical Engineering
University of California, Riverside, September 2012
Professor Cengiz Sinan Ozkan, Chairperson

Realistic implementation of graphene and carbon nanotubes (CNT) in energy devices and nano-electronics requires these carbon nanomaterials to have engineered architectures with sp^2-hybridized carbon atoms as building blocks. Graphene-CNT hybrid structures will provide attractive material properties of both CNTs and graphene with the capability to develop into a variety of geometries. The first part of this dissertation presents a scalable approach for synchronous fabrication of multiple component carbon hybrids. Large and uniform graphene-CNT hybrid films are successfully synthesized via simultaneous CVD growth of graphene layers and CNTs on copper foil substrates. The graphene-CNT hybrids have tuneable nano-architectonics, which is essential for application-oriented design of hierarchical graphene structures. The unique mechanism of synchronized CVD growth of CNT and graphene contributed significantly to the composure of the final carbon structure. We also demonstrate the potential of Block Copolymer (BCP) self-assembly as a nano-fabrication and patterning tool. Block copolymers are

employed as templates to fabricate desired arrays of catalyst particles for CVD growth. Thoughtful choices of constituent blocks, polymerization degree, and volume fractions in BCPs, enable us to modulate the size and the separation distance of micro/nano-domains in the coplymer templates. Such versatility provides us with a powerful tool to control the diameter and separation distance of grown CNTs in the pillared architectures, and eventually allows us to tune the surface area in the resulting carbon hybrids.

The metrology part of this work focuses on the utilization of fluorescence quenching microscopy (FQM) for quick visualization of doping in large-area graphene layers. Reactive ion plasma etching allows us to generate patterns of p-type CVD-grown graphene layers doped with fluorine. We specifically employ the dye 4-(dicyanomethylene)-2-methyl-6-(4-dimethylaminostyryl)-4H-pyran (DCM) as the fluorescent agent. The emission of DCM is quenched to different extents by p-doped and non-doped regions of graphene. This provides the fluorescence-imaging contrast, which is critical for visualization/mapping of the doped regions in high-throughput metrology techniques. To determine the method's resolution and scalability strengths, we increased the complexity of the doping pattern and successfully reproduced the mapping results. Upon that, we conducted a comparative investigation on steady-state and time-resolved fluorescence parameters of dye-coated pristine graphene and fluorinated graphene, using bare glass as the control sample. Fluorometry results support the increasing trend observed in the quenching level of DCM dye, from control sample to doped graphene

to pristine graphene. The variation in fluorescence quenching by graphene after it is doped is also predicted by theory, as discussed in this work. Due to its simplicity, high speed, and small footprint, segmented FQM can be employed to address the chronic need for a microscopy based graphene metrology capable of “seeing” the features that are processed.

Content

List of Figures

List of Tables

Chapter 1

1. Introduction

As the industry demands more and more sophisticated solutions from applied sciences, there is an ever-growing need for new materials with performance improvements over the traditional materials. Today, breakthroughs in industrial fields are often associated with development of novel materials, which change not only the possible solutions but also the very nature of the technological problems. In the semiconductor industry, a standard example of the aforementioned trend, fabrication and implementation of new devices relied heavily on innovative materials solutions. Successful development of such solutions often calls for high-throughput manufacturing approaches, and new metrology techniques to provide feedback to the fabrication process. Therefore, as industry moves ahead in the realm of novel materials, nanomanufacturing and metrology are expected to play more decisive, yet challenging roles.

Graphene is a new carbon material that has been hailed as the latest prodigy of nanotechnology, and eventually claimed a Physics Noble prize in 2010. Such a contagious academic sensation has been primarily caused by graphene's fascinating and versatile properties such as high charge carrier mobility, unique band structure, mechanical robustness, high thermal transport, and chemical stability.[1-7] As a result, there has been a considerable amount of theoretical and experimental research dedicated to potential applications of graphene nanostructures in field-effect transistors, actuators, solar cells, batteries, and sensors.[8-11] For graphene, however, to successfully transition from a gifted child into an accomplished adult that delivers its promises, it still needs to be fabricated in industrially-usable large sheets.

Carbon nanotubes (CNTs), another class of carbon nano-material, have also been the subject of intensive research over the last two decades because of their exceptional electronic, optical, mechanical and chemical properties.[12-14] Several outstanding features such as outstanding electronic transport, the ability to carry large current densities, high aspect ratio and fast electron-transfer kinetics, make CNTs appealing for applications in electrochemical sensing, energy storage, field-emission devices and photovoltaics. [15-18]

For a realistic application of graphene and CNTs in many of the above-mentioned applications there is a need for graphene layers to have engineered architectures with sp^2-hybridized carbon atoms as building blocks. Such conceived graphene-CNT hybrid structures will combine attractive material properties of both CNTs and graphene with the capability to develop a variety of geometries. This versatility makes sp^2 hybrid carbon materials ideal candidates for a number of applications including nanoelectronics, energy conversion and storage, sensors, and field emissions. The common requirements in these applications are carefully engineered architectonics, and nanoscale assembly of different building blocks of desired hybrid structure. Such material nano-engineeering is challenging due to strong Van deer Waals interaction between sp^2 graphitic materials that yields restacking of graphene layers and bundling of carbon nanotubes. Therefore, devising a fabrication methodology for spatial distribution of graphene layers and CNTs in hybrid carbon architectures is crucial and rewarding.

In **chapter 2** we report on the successful synthesis of a graphene-carbon nanotube (CNT) hybrid architectures by a synchronized chemical vapor deposition of the two carbon allotropes. The carbon hybrid is a three-dimensional nanostructure with tuneable architecture comprising vertically grown carbon nanotubes as pillars and a large-area graphene plane as the floor. The formation of CNTs and graphene occurs simultaneously in a single CVD growth step that we describe as a synchronous synthesis methodology. Unique nature of the fabrication approach contributes significantly to the quality and composure of final nano-hybrid. Detailed characterization elucidates the cohesive structure and seamless contact between the graphene floor and the CNTs in the hybrid structure. We also demonstrate the functionality of our fabricated PGN structure by featuring a supercapacitor PGN cell. It is noteworthy that the new PGN based supercapacitor was not achievable for graphene-CNT hybrids synthesized on Si/SiO2 substrate as silicon platform is nonconductive and brittle. Our fabrication approach provides a practical pathway for the fabrication of novel 3-D hybrid nanostructures, and efficient device integration that bridge graphene-CNT hybrids from laboratory to industry level applications.

Tto achieve desired structure/properties for industrial applications, tt is critical to tune the architecture of graphene-CNT structures at nanometer-scale. This requires a method for fabrication and patterning of catalyst nanoparticles arrays on the growth substrate. The catalyst particles are being used as seeds for growing carbon nanotubes through chemical vapor deposition and therefore are being considered as the cornerstone of desired nanostructures. The interest here lies in producing and patterning arrays of catalyst particles with controlled size and separation distance that result in controlled diameter and separation distance of grown carbon nanotubes, and eventually controlled amount of final active area.

In **chapter 3**, we demonstrate utilization of Block Copolymers (BCP) for fabrication of the catalyst arrays foundation of pillared graphene nanostructures. First, we describe the concept of microphase separation that results in self-assembly phenomena in BCPs. Next, we discuss how BCPs can assemble into a range of well-defined and ordered structures depending on the volume fractions of their components. Moreover, we experimentally demonstrate that the molecular weight of the copolymer provides control over the size and separation distances of the polymer nano-domains. Unique functionality can be added into the BCP structure by varying the chemical nature of the copolymer blocks. This capability makes block copolymers ideal candidates for nanofabrication and patterning templates of targeted nanostructures. In the remaining parts of chapter 3 we demonstrate BCP-based strategies to fabricate and tune carbon nanostructures.

Size and scalability are the primary obstacles for widespread industrial use of graphene. Most promising applications of graphene, such as solar cells an d batteries, require reliable and wafer-scale metrology. Common techniques for characterizing graphene are Raman spectroscopy, scanning probe microscopy, and X-ray photoemission spectroscopy. While these techniques provide valuable information about electronic and structural properties of graphene at an atomic-level, they are often slow and can only cover small regions; this is not ideal for the large-area graphene samples produced by CVD or chemical reduction.

The greatest challenge in employing graphene industrially, in areas such as energy, semiconductor fabrication, and thermal management, has been making it viable at larger scales. This requires making graphene industry-ready by developing an industrial metrology technique that has a small footprint, and can characterize large-scale graphene samples with high speed.

In **chapter 4,** we describe the utilization of fluorescence quenching microscopy (FQM) for quick visualization of doping in relatively large regions of graphene, grown via chemical vapor deposition (CVD). Through reactive ion plasma etching, we generate patterns of p-type CVD-grown graphene doped with fluorine. We employ 4-(dicyanomethylene)-2-methyl-6-(4-dimethylaminostyryl)-4H-pyran (DCM) as the fluorescent agent. The emission of DCM is quenched to a different extent by p-doped and non-doped graphene, which provides the fluorescence-imaging contrast essential for this metrology. To probe the doped surface patterns with DCM, we disperse the dye in polymethylmethacrylate (PMMA) then coat the graphene surface, forming a 30-nm-thick DCM-PMMA layer. Fluorescence images of dye-coated graphene distinctly reveal the difference between the doped and non-doped regions. The non-doped graphene quenches the DCM emission more efficiently than the doped graphene. Therefore, the regions with non-doped graphene appear darker on the fluorescence images than the regions with doped graphene, enabling large-scale mapping of the doped regions in CVD grown graphene sheets. Through Gaussian curve fitting of the image histogram, we segment the fluorescence image into different graphene regions. Steady-state and time-resolved absorption and emission spectroscopy are used to comparatively characterize the photophysical properties of the dye when immobilized in PMMA films coating bare glass, pristine graphene, and doped graphene. We observe that a three-fold increase in the in the rate constant of non-radiative decay is the principal reason for the DCM fluorescence quenching for the graphene regions of the samples. The spectral overlaps reveal the propensity for energy transfer from DCM to graphene, causing the increase in the rates of non-radiative deactivation of the photo excited dye. Due to its simplicity and consistent results, FQM is now poised for widespread adoption by graphene manufacturers as a basis for facile and high throughput metrology of large-scale graphene sheets.

1.1 References

[1] K. S. Novoselov, A. K. Geim, S. V. Morozov, D. Jiang, M. I. Katsnelson, I. V. Grigorieva, S. V. Dubonos, A. A. Firsov, *Nature* **2005**, *438*, 197.

[2] K. S. Novoselov, A. K. Geim, S. V. Morozov, D. Jiang, Y. Zhang, S. V. Dubonos, I. V. Grigorieva, A. A. Firsov, *Science* **2004**, *306*, 666.

[3] Y. Zhang, Y.-W. Tan, H. L. Stormer, P. Kim, *Nature* **2005**, *438*, 201.

[4] A. K. Geim, K. S. Novoselov, *Nat. Mater.* **2007**, *6*, 183.

[5] J.-H. Chen, C. Jang, S. Xiao, M. Ishigami, M. S. Fuhrer, *Nat Nano* **2008**, *3*, 206.

[6] A. A. Balandin, S. Ghosh, W. Bao, I. Calizo, D. Teweldebrhan, F. Miao, C. N. Lau, *Nano Lett.* **2008**, *8*, 902.

[7] C. Lee, X. Wei, J. W. Kysar, J. Hone, *Science* **2008**, *321*, 385.

[8] F. Schedin, A. K. Geim, S. V. Morozov, E. W. Hill, P. Blake, M. I. Katsnelson, K. S. Novoselov, *Nat. Mater.* **2007**, *6*, 652.

[9] X. Wang, L. Zhi, K. Mullen, *Nano Lett.* **2007**, *8*, 323.

[10] J. Yan, T. Wei, B. Shao, Z. Fan, W. Qian, M. Zhang, F. Wei, *Carbon* **2009**, *48*, 487.

[11] E. Yoo, J. Kim, E. Hosono, H.-s. Zhou, T. Kudo, I. Honma, *Nano Lett.* **2008**, *8*, 2277.

[12] S. Iijima, *Nature*, 1991, **354**, 56-58.

[13] M. S. Dresselhaus, G. Dresselhaus and A. Jorio, *Annual Review of Materials*, 2004, **34**, 247-278.

[14] Popov and N. Valentin, *Materials Science and Engineering*, 2004, **43**, 42.

[15] P. G. Collins, M. S. Arnold and P. Avouris, *Science*, 2001, **292**, 706-709.

[16] A. Javey, J. Guo, Q. Wang, M. Lundstrom and H. Dai, *Nature*, 2003, **424**, 654-657.

[17] W. A. de Heer, A. Chatelain and D. Ugarte, *Science*, 1995, **270**, 1179-1180.

role.

Chapter 2

2. Synchronous Chemical Vapor Deposition of Large-Area Hybrid Graphene-CNT Architectures

2.1 Introduction

Graphene-CNT hybrid structures will combine attractive material properties of both CNTs and graphene with the capability to develop a variety of geometries. This versatility makes sp^2 hybrid carbon materials ideal candidates for a number of applications including nanoelectronics, energy conversion and storage, sensors, and field emissions.[19-26] The common requirements in these applications are carefully engineered architectonics, and nanoscale assembly of different building blocks of desired hybrid structure. Such material nano-engineeering is challenging due to strong Van deer Waals interaction between sp^2 graphitic materials that yields restacking of graphene layers and bundling of carbon nanotubes. As a result it is necessary to develop fabrication technique for assembly of graphene sheets and CNTs in hybrid carbon architectures.

The method by which graphene is prepared is critical in functionality of the synthesized carbon hybrid. For example, in hybrids that are constructed from reduction of graphene oxides, there are serious concerns regarding the uniformity and quality of resultant graphene layers.[27] These problems would be pronounced in resulting graphene hybrid structures in form of poor controllability of the nano-architecture and remarkable reduction of surface area, which is a key property of carbon hybrids. Alternatively, when graphene layers are prepared by mechanical exfoliation of graphite or graphite oxide, there are some serious limitations in terms of scalability, reproducibility, and mass fabrication.[2] While the quality of mechanically cleaved graphene in some micron-sized flakes is superior, mechanical exfoliation is size-limited and incapable of volume production of large scale graphene. Another problem of this approach stems from separate synthesis of CNT and Graphene in the fabricated carbon hybrid. In this context, Fan *et al* utilized exfoliated graphene oxide layers along with CVD grown CNTs to fabricate CNT/graphene sandwich.[28] While this approach shows a good potential for lab-scale synthesis of hierarchical nanostructures, its applicability could be enhanced by addressing scalability problems and consistency issues between CNT and graphene that are synthesized with different methods.

It is clear that large-area synthesis of uniform graphene layers is critical for incorporation of graphene-based structures into nano- and opto-electronic devices.[29, 30] Among the various approaches for the synthesis of carbon nanotubes and graphene sheets Chemical Vapor Deposition (CVD) shows the highest capacity for large-scale production due to its large throughput, controllability, reproducibility, and capability to deliver in situ growth. While other fabrication approaches, grown nanotubes or graphene should be extracted and transferred, CVD based methodologies can grow directly on the desired substrate. The CVD-grown structures are controllable through careful selection and assembly of the catalyst layers. Repeated reports on CVD grown graphene show that the large-area monolayer graphene film can be grown directly on the nickel and copper surfaces by carbon precipitation or surface-catalyzed mechanism, respectively.[31-34]

The assembly methodology is another important part of the fabrication procedure that substantially affects the quality and applicability of the graphene-CNT hybrids. Within recent years, studies have been aimed towards fabricating hybrid carbon films by surface functionalization, and self-organizing of homogeneously mixed solution of dispersed CNTs and reduced graphene oxides. The major advantage of this approach is its scalability and large throughput.[21, 22] Nevertheless, the hybrid films prepared by such method contain considerable amount of restacked graphene and CNT aggregates, resulting in poor controllability of the hybrid nanostructure and reduction of total active surface area. Furthermore, generally in all assembly approaches that involve detachment and transfer of CNTs from the growth substrate to another location or structure, the resulting electrical and mechanical contact in the assembled structure would be low.

Another major approach for graphene-CNT assembly was the growth of CNTs on the reduced graphene oxide film, carried out by Lee et al.[19, 25, 26] In this method, block copolymers has been applied to create uniformly patterned metal catalyst arrays for CNT growth in the carbon hybrid. This creative approach is a technical improvement that produces better electrical contacts and more efficient device integration. In this context, Dong *et al* studied one-step growth of graphene-carbon nanotube hybrids by coating silicon nanoparticles on copper foil and using ethanol vapor as carbon source.[35] The parallel growth of graphene and CNTs increases the potential of this technically attractive approach to improve the quality of contact between CNTs and graphene, as their synthesis is similar in nature. The adopted approach relies on introducing an extra material, Si nanoparticles, for the synthesis of carbon nanotubes. This yields dependence of CNT growth sites on sporadically decorated Si nanoparticles that may influence the uniformity and density of CNTs in the hybrid.. Altogether, it seems in almost all synthesis scenarios for graphene-CNT hybrids the vertical CNTs are either transferred from their growth substrate (primarily flat dielectric oxide substrate) or grown by an entirely different fabrication step.

Herein, we aim to depart from serial approaches, where the synthesis of hybrid nanostructures is carried out by sequential addition of different components of the final composite structure, into a well-designed single-step growth. We demonstrate large-scale synchronous synthesis of graphene and carbon nanotubes into Pillared Graphene Nanostructure (PGN) on the copper foil for the first time. The initial idea of such 3-D carbon networks was sparked by theoretical studies aiming at introducing novel energy storage assemblies based on tuneable and large surface area nanostructures.[23] While in our first experimental attempts[36]PGN was grown on lithographically patterned, copper evaporated Si/SiO$_2$ substrate, here for the first time we report large-scale synthesis of this carbon hybrid on plain copper foil. This is a major technological step-up since for all applications in general, and for energy storage devices in particular, the substrate materials for PGN growth needs to be flexible, geometrically adjustable, and conductive. Moreover, in our new synthesis technique the need for lithography pre-patterning of the growth substrate, part of experimental procedure of previous fabrication approach[36], has been removed. As a result, the fabrication method has upgraded from a “serial” to a large-scale “parallel” technique. Due to the integrated nature of the synthesis method, the resulting hybrid structure shows a superior cohesion and crystalline contact between graphene and CNT building blocks. We also demonstrate the functionality of our fabricated PGN structure by featuring a supercapacitor PGN cell. It is remarkable that the new PGN based supercapacitor was not achievable for graphene-CNT hybrids synthesized on Si/SiO2 substrate as silicon platform is nonconductive and brittle. With its scalability, efficiency, and simplicity, our new methodology bridges Graphene-CNT hybrids from laboratory to industry level applications.

2.2 Experimental Work

Graphene-CNT Synthesis Procedure: 25 μm thick copper foils (from Alfa Aesar, cut into 1cm$_2$ area) were chosen as the substrate material. An Oxygen plasma treatment (STS Reactive Ion Etcher) was carried out on the copper foil strips surface at 200 W and 100 mTorr for 90 s to create a barrier oxide layer on copper foil. Fe catalyst films with a thickness of 3-5 nm were then deposited on copper oxide using electron beam evaporator (Temescal, BJD-1800). Next, growth foils were loaded into a CVD chamber and heated to 750°C under the flow of 500 sccm of Ar. All flow rates were precisely controlled by using mass flow controllers. To make the velocity profile of gas flow more uniform a total pressure of 650 Torr is maintained in the CVD tube. Once the temperature is stabilized at 750°C, first 100 sccm of H_2 is initiated, and after 5 mins 50 sccm of C_2H_2 is introduced into the tube for 10 to 20 min to begin the synthesis of graphene-CNT hybrid. Upon completion of the CVD growth, C_2H_2 and H_2 gas feeds were stopped, and the furnace was cooled to the room temperature under the protection of Ar gas flow. If needed, graphene-CNT hybrid films were removed from the Cu film by etching in a 1M aqueous FeCl3 solution, followed by cleaning with an aqueous HCl (5%) and D.I. water solution. Subsequently, pillared graphene films were collected from the D.I. water with a substrate of choice.

Characterization: Detailed characterization of the synthesized CNT-graphene hybrid films and catalyst surfaces were performed using optical microscopy, Scanning Electron Microscopy (SEM; Leo, 1550), and Transmission Electron Microscopy (TEM; Philips, CM300) with a LaB_6 cathode operated at 300kV and equipped with an X-ray energy-dispersive spectroscopy (EDS) module. TEM samples were prepared by collecting the etched graphene-CNT films suspended on

D.I. water, with a TEM copper grid. Electron diffraction patterns on the graphene-CNT films change from one location to another. The main difference observed is the appearance of other sets of hexagonal spots and the amplification of the ring patterns on the locations with dense CNT growth. Raman spectra were taken with a ThermoFisher Scientific micro-Raman equipped with DXR 532-nm Excitation Laser Set. Most spectra were taken in more than four spots to guarantee the reproducibility of the peak intensities.

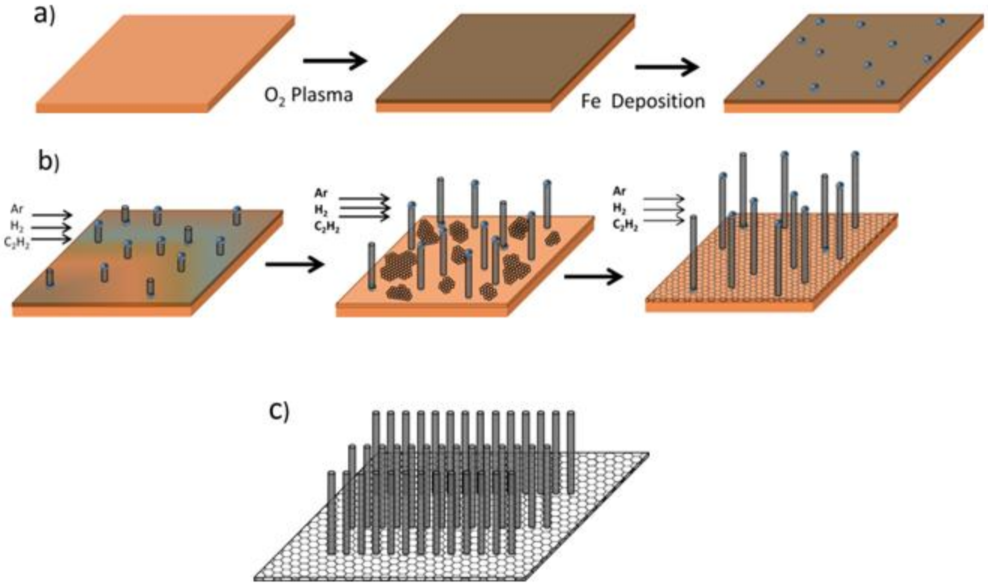

Figure 2-1 Schematic diagram of (a) preparation of the growth substrate and the catalysts: oxygen plasma treatment of the copper foil followed by iron deposition. (b) Probable mechanism of synchronous growth of CNTs and underlying grapheme. (c) Pillared graphene hybrid structure comprising vertically grown carbon nanotubes as pillars and large-area graphene plane as a floor.

Preparation of Supercapacitor Test Assembly: To prepare PGN-Supercapacitor Cells the as grown PGN films with copper substrates were cut into equal areas and assembled in split flat cell (MTI EQ-STC). Gamry Reference 600™

was used as electrochemical analyzer for capacitance measurement. Regular filter paper (Whatman 8-um filter paper) were soaked with the electrolyte (2 M Li_2SO_4 solution) and was used as separator.

2.3 Synchronous Synthesis of Graphene and Carbon Nanotubes

Pillared graphene is a spatial carbon network consisting of CNT pillars grown vertically from large-area graphene planes. This carbon hybrid structure looks like a building under construction, with carbon nanotubes as the pillars and graphene sheets as the floor (Figure 2-1). The schematic in the Figure 2-1a is also illustrates the process used to prepare the growth substrate before the synchronous synthesis. As discussed in the experimental section, Fe particles, “seeds” for CNT growth, were e-beam evaporated on a layer of copper oxide prepared by O2 plasma treatment of copper foil. We first investigate the CVD growth of CNTs on the processed copper substrate, and then look into the entire perspective on the synchronous synthesis of the cabin hybrid.

As opposed to copper-based CVD growth of graphene, which could be considered experimentally established technique by now [33, 34], the synthesis of carbon nanotubes on copper surface is challenging due to the undesired interaction between the metallic catalysts regularly used for carbon nanotubes (mainly Fe, Co, and Ni) and copper . The main technique used to overcome this obstacle is to deposit an intermediate layer between metallic catalysts and Cu surface to act as a diffusion barrier.[37-40] However, adopting this approach for the CNT-graphene hybrid case introduces extra buffer materials that are hard to remove and tend to stay in the final hybrid structure. This consequently affects the functionality of the carbon hybrid structure, particularly in applications that strongly depend on the composition of the nanostructure used. Such barrier layers would also restrict the exposure of the copper layer to the flow of carbon source gas that is fundamental in our methodology.

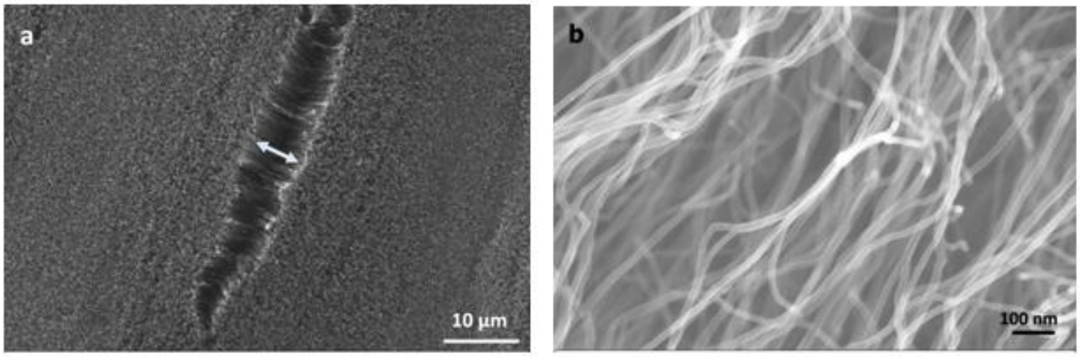

Figure 2-2 (a) Top-veiw SEM micrograph of CNT pillars in CNT-graphene hybrid, grown on pre-oxidized copper foil. The image showing dense and vertically aligned growth of CNT pillars on graphene sheet. (b) Higher magnification SEM micrograph of the CNTs reduced back to zero-valent copper. This finally leads to exposure of the pure copper to acetylene.

It is necessary to develop a barrier layer that can be removed or consumed in the course of growth. To address this problem we devise a step of oxygen plasma pre-treatment to form a controlled layer of copper oxide on top copper foil, separating it from to-be-deposited CNT catalysts. Copper oxide could be reduced during the growth while hydrogen flow is introduced. Hydrogen reduction of the copper oxide is essentially possible since copper stands below hydrogen in reactivity series. The high temperature inside the CVD chamber significantly facilitates this reaction. Therefore, as the CNT starts growing from the surface of the copper-copper oxide foil, the oxide layer would be gradually flow, the carbon source gas, and the formation of the graphene layer in parallel with the CNTs' growth. To achieve realistic mass production technique and reduce the complexity of the fabrication, in our new synthesis approach the need for lithography pre-patterning of the growth substrate, a necessary part of previous fabrication approach, has been removed.[36] Figure 2-2a displays a typical top-view SEM micrograph of a large area CNT-graphene hybrid layer. The gap in the surface, marked with a double arrow, allows us to see the vertical direction of the CNT growth. This figure also shows the uniform morphology of grown CNTs over the large area of the hybrid film. Figure 2-2b is a higher magnification SEM indicating the average diameter of CNTs to be less than 20nm with narrow size distribution. To achieve a better understanding of the role of oxide layer in the synthesis, we conducted a comparative study on two similar copper foils, with and without O_2 plasma treatment.

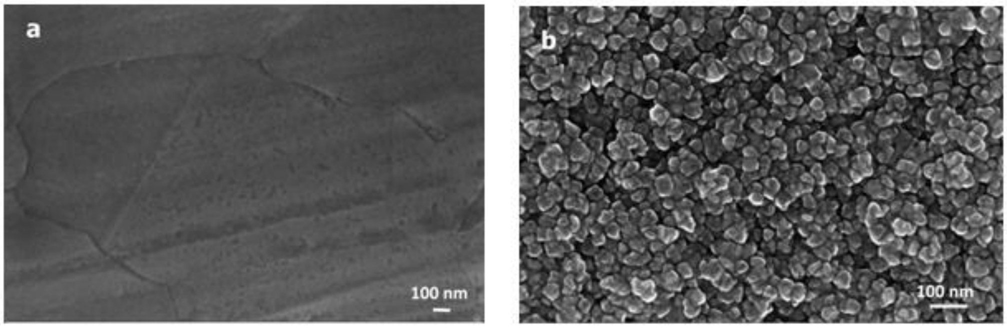

Figure 2-3 SEM images of copper substrate (a) before, and (b) O2plasma

Figure 2-3a and 2-3b shows SEM micrographs of the surfaces of the copper foil samples unmodified and after O_2 plasma treatment, respectively. Figures 3a and 3b show the SEM images of (a) unmodified copper, and (b) plasma treated copper surfaces after deposition of 4nm iron followed by CVD process with hydrogen and acetylene. Comparison between Figures 2-3a and 2-3b suggests that the oxygen plasma treatment dramatically changes the morphology and size of the surface grains. It appears that through conversion of copper grains to copper oxide grains, oxygen plasma treatment increases surface roughness and accordingly poses more grains and larger surface area. This produces higher level of surface energy, which consequently results in more active nucleation sites for the CNT growth on the surface. Indeed, according to nucleation and growth theory the higher the energy of the nucleation sites, it is more likely to have higher number of stable embryos on the surface.[41, 42] Moreover, considering the total energy of the system for nucleation and growth, more stable nucleation sites results in more unilateral growth.[41, 43] Figure 2-4b shows SEM image of the same copper foil (Figure 2-3b) after Fe deposition and CVD process. It is clear that the plasma-treated copper foil substrate gives rise to dense growth of carbon nanotubes with vertical alignment, as opposed to unoxidized copper layer. The oxide layer can also play the role of a barrier, impeding the unfavourable Fe-Cu interaction by separating two catalyst metals. As it can be seen from Figure 2-4a, the unoxidized Cu foil would hardly give rise to any carbon nanotubes without any barrier layer. This may be explained by the increasing interaction between Fe and Cu and the possibility of the formation of metal solid solution due to nano-scale sizes of Fe particles and high growth temperature.[38, 44] Furthermore, the grown CNTs from this substrate would be much larger in diameter and shorter in length as the sparse nucleation sites allow lateral growth of CNTs.

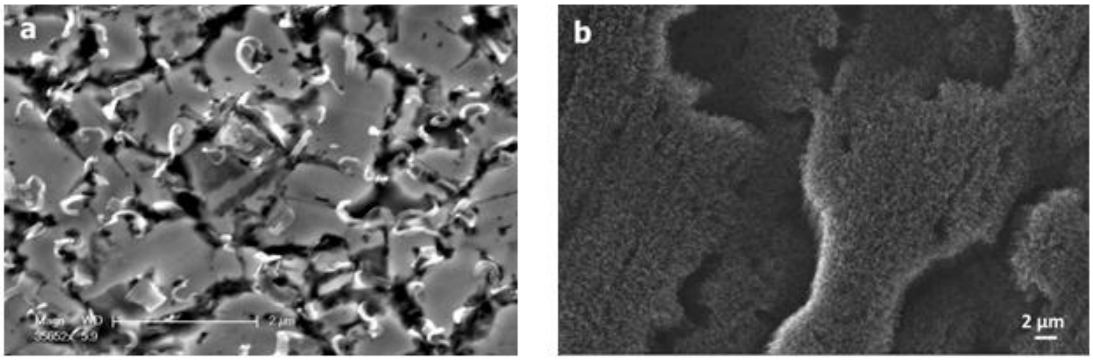

Figure 2-4 SEM images of PGN grown on (a) regular, and (b) pre-oxidized copper foil, showing dense and aligned growth of CNT pillars on graphene sheet.

The records of our synthesis attempts suggest that an optimized recipe for copper oxidization pre-treatment is critical for the growth of the CNT-graphene hybrid. In fact, even small violations from optimized oxygen plasma specifications could affect the quality of the growth substantially. This could be explained by the significance of the average grain size and the roughness of the growth surface which depends on oxidization conditions. It should be noted that there is very fine balance between the thickness of the oxide layer and the CVD growth conditions, as the hydrogen flow and growth temperature determine the reduction rate of the oxide layer. This additionally points to fundamental role of the hydrogen gas flow in CVD growth of pillared graphene. Similar to what discussed for hydrocarbons catalytic decomposition, hydrogen molecules dissociate in the presence of metallic catalysts and at the growth temperature of around 750K.[45, 46] The resulting atomic hydrogen is very reactive and tends to act as an etching agent for carbon, in addition to reducing copper oxide. Therefore, if the selected ratio of acetylene to hydrogen flow is too low, the etching reaction becomes faster than formation sp2 carbon hybrids. The hydrogen flow contributes to the "growth" part through its role in production of reactive hydrocarbon.[31-34, 45]

Figure 2-1 illustrates a probable formation process of the pillared graphene hybrid in one-step CVD growth. First, the iron deposited copper foil is exposed to the flow of H_2, C_2H_2, and Ar gasses as described in the experimental section. As CNT nucleation sites form on the copper oxide surface, hydrogen flow start reducing copper oxide layer as displayed by the change of colour on copper oxide layer in the schematic. Next, the oxide layer is completely reduced by hydrogen flow and consequently graphene islands begin to form via surface-catalysis mechanism induced by the exposure of copper to carbon source gas.[33, 34] Meanwhile CNTs continue to grow vertically. Finally, the graphene layers cover the substrate and merges with CNTs at their roots on the substrate plane.

To gain a deeper insight into the probable synthesis process of pillared graphene hybrids, we consider the CVD growth mechanisms of CNTs and graphene in further detail. In catalytic growth of CNTs by CVD, a metallic catalyst particle, Fe in our case, decomposes the hydrocarbon molecules of a source gas and absorbs carbon atoms to its structure, until it becomes carbon-saturated. The absorbed carbon atoms diffuse through the bulk body of the catalyst particle and upon saturation, precipitate from the other side to form cylindrically rolled graphene layers.[47] Strong catalyst-substrate interaction results in base-growth mode, where catalysts remain on the substrate; and weak catalyst-substrate interaction yields tip-growth mode, in which catalyst remain on the tip of the growing CNT.[47, 48]

The synthesis mechanism for CNT pillars in graphene hybrids is more complicated since it involves the simultaneous growth of graphene and CNTs. In the pillared graphene synthesis, while the CNTs start to grow through the above-mentioned mechanism, copper oxide layer formed by O_2 plasma pre-treatment is gradually reduced by hydrogen flow until copper atoms resurface and are exposed to acetylene flow in the CVD chamber. Subsequently, the graphene films directly grow on the Cu surface by a surface-adsorption mechanism. It is noteworthy that in the copper-based graphene synthesis graphene is growing by a surface-catalyzed mechanism rather than carbon precipitation process that is attributed to grapheme CVD growth by nickel.[31-34]

Considering the overall perspective on the synthesis of pillared graphene, the “floor” graphene grows through carbon nucleation sites. They form by catalytically adsorption of carbon to copper and grow horizontally with the addition of carbon to their boundaries.[33, 34] The graphene nucleation sites continue expanding by adsorption of more decomposed carbon atoms to their edges, until graphene domains join and form a graphene sheet.[33] In the meantime, the growing planar graphene islands join cylindrically rolled graphene layers, CNTs, at their interface with the substrate, developing pillared graphene nanostructure.

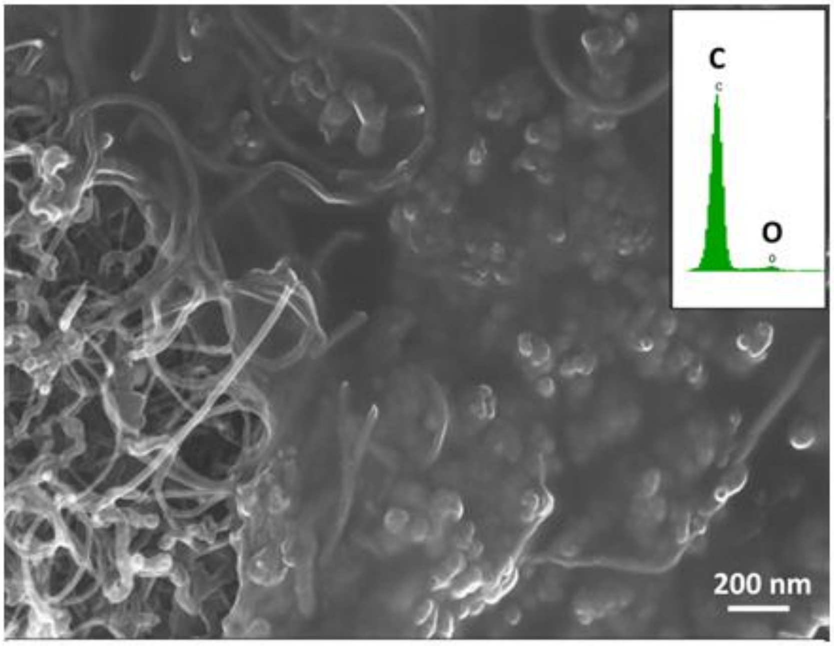

Figure 2-5 Bottom-view SEM micrograph of the backside of the peeled PGN film, showing the graphene film embedding CNT pillars roots

The copper-based graphene growth also allows a more time-flexible exposure of the metallic catalyst to carbon source gas. This is crucial to our synchronous fabrication, as we require simultaneous growth of graphene and CNTs for pillared graphene hybrid. Using coppers layer catalyst also intrinsically yields more uniform graphene with fewer layers.[33, 34] As it mentioned before, excess hydrogen flow rate could be counter-productive as it removes copper oxide barrier prematurely and thus reduces iron catalysts activity and lifetime through possible Fe-Cu interaction at some CNT nucleation sites. Other probable drawback of surplus hydrogen flow is the overexposure of copper foil to hydrogen that affects the quality of graphene layer in the hybrid.

2.4 Characterization of the Synthesized Hybrid Graphene - Cabon Nanotube Structure

Further study of the synthesized pillared graphene provides a deeper insight into growth mechanism of carbon hybrids, and paves the way for their application-oriented fabrication. Figure 2-5 gives an interesting view of the "back side" of a synthesized graphene-CNT hybrid. To obtain this bottom-view image, the grown hybrid film was peeled using a double sided carbon tape, and then placed onto SEM sample holder. The image displays how CNTs roots are embedded in grapheme sheets. This is an important observation which further indicates the cohesion of the hybrid pillared grapheme architecture where CNT "pillars" are connected to graphene "floor". The EDS spectra taken from the backside of the sample verifies carbon as the "floor" material. The SEM image and the fact that carbon tape peeled the whole CNT-graphene hybrid rather than only CNTs, indicates a robust mechanical connection between synchronously synthesized CNTs and graphene. Figure 2-6a displays an optical micrograph of a pillared graphene sample transferred onto SiO_2/Si substrate. To remove the pillared graphene structure from copper foil the underneath Cu attachment was etched using 1M aqueous $FeCl_3$ solution. Subsequently the PGN sample was cleaned by HCl solution/ D.I. water, and then collected by the SiO_2/Si substrate.

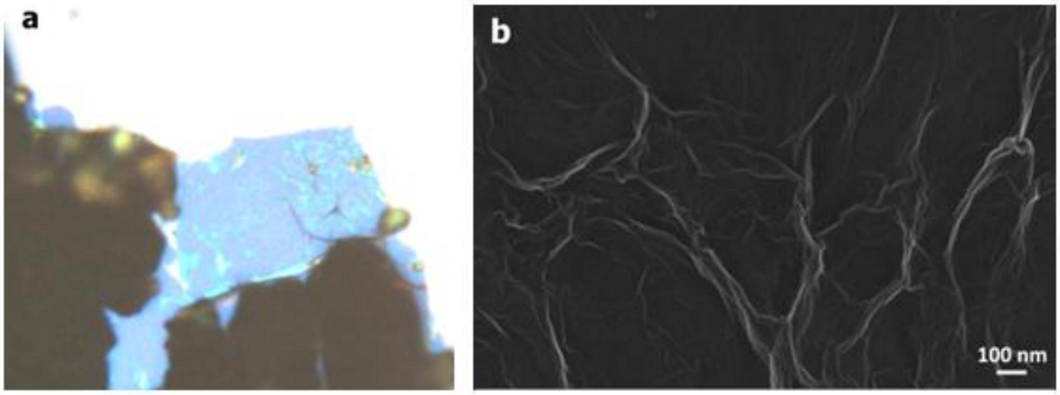

Figure 2-6 (a) Optical micrograph of PGN structure. Partial growth of CNTs reveals graphene underlying film and shows the PGN structure. (b) High magnification SEM micrograph of graphene film in graphene-CNT hybrid

The optical micrograph was taken of a selected area of PGN that is partially covered by as-grown CNTs (due to scarce to zero presence of Fe catalysts), and thus it reveals the underlying graphene sheet, blue area, under the CNTs. Figure 2-6b shows the SEM image of the graphene layer in the same PGN sample. As it is expected the graphene layer contains wrinkles which are mainly caused by mismatch in the thermal expansion coefficient between copper and graphene.33A Typical Raman spectrum taken from CNTs in the pillared graphene is shown in Figure 2-7a. The G band, centered on 1570 cm-1, is the first order Raman mode induced by in-plane vibration of carbon atoms in sp2 hybridized graphene sheets. As a result, the intensity and sharpness of G band is signifying the presence of crystalline graphitic phase in the synthesized material. The D band at 1335 cm-1, on the other hand, is the defect originated second order Raman band which indicates the level of defects in graphitic sp2 structures. The nature of this band is related to one-phonon elastic scattering and it is interpreted as a measure of the quantity of sp3 or dangling sp2 bonds that are causing structural disorders. Thus, the ratio of D band and G band peak intensities, I_D/I_G, is commonly agreed as a gauge of the quality of CNTs and in general all graphitic materials. The lower values of this ratio show the superior grade of carbon structure and fewer amounts of amorphous carbon disorders and defects. The average value of this ratio taken from our samples is 0.82 which is lower than the values reported from similar studies on the CVD grown CNTs on copper substrates.[37, 38, 40] The higher quality of PGN structure compared to regular CNTs grown on copper substrate may be explained by the different strategies adopted for the synthesis and in particular the effect of intermediate layers.[37, 38] While we oxidized a thin layer of copper substrate itself to serve as the buffer layer, the general approach is deposit an external intermediate layer as a barrier film on the copper substrate before the CNT growth. This demonstrates the advantage of copper oxide layer in terms of simplicity and final products' quality. The Raman spectra did not show any appreciable radial breathing mode (RBM) peak which indicates that grown CNTs are mostly multiwalled. Figure 2-7b is a Raman spectrum of graphene sheet in PGN sample. The spectrum, which is taken from areas with no CNT pillars, confirms bi-to few layer graphene as the "floor" material of the hybrid structure.

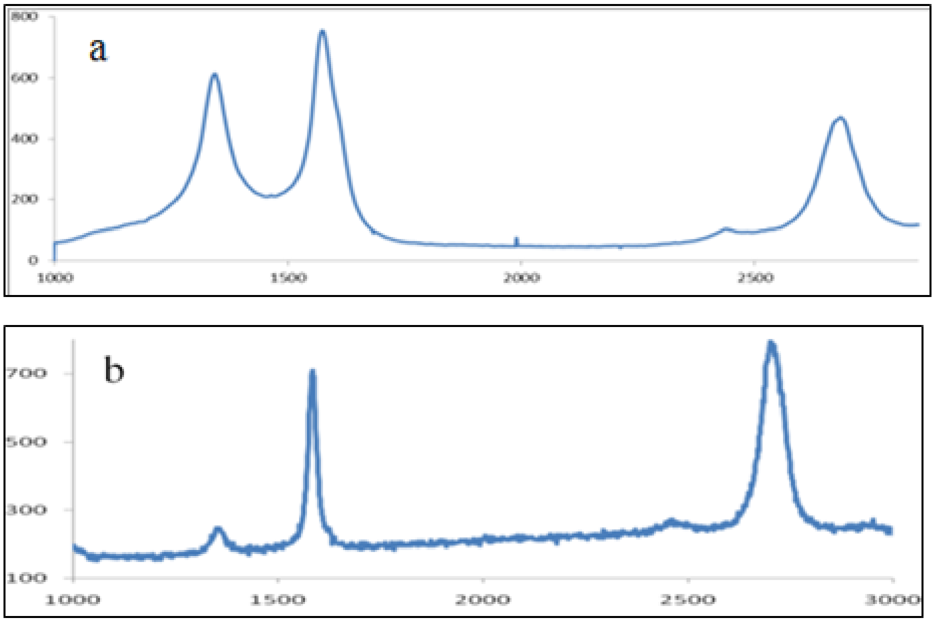

Figure 2-7 (a) Typical Raman Spectra of PGN showing the presence of D, G, and 2D band centerd around 1335 cm^{-1}, 1570cm^{-1}, and 2672cm^{-1} respectively (Thermo Fisher DXR micro Raman, λ_{laser} = 532 nm). (b) Raman spectra of the graphene layer in PGN film grown on copper foil.

Figure 2-8 shows a TEM image the of pillared graphene film synthesized from deposited copper layer. To prepare TEM sample, first the graphene-CNT film was etched from copper using Ferric Chloride and Hydrochloric solutions. The suspended hybrid film is then collected from D.I. water by a suitable copper grid. The TEM image shows the graphene-CNT hybrid through the underlying graphene. This is a very informative image allowing us to look into the interface between CNT pillars and graphene floor of the carbon hybrid. First, the recurring circular hollow patterns in the interface of a CNT and graphene layer, shown with red circle marks, confirm that CNTs' roots are embedded in the graphene sheet. This further indicates the smooth transition between the two carbon allotropes, graphene and CNTs, in the hybrid structure. The Energy Dispersive Spectrum (EDS) taken from the dark spots at the tips of CNTs verifies them as Fe catalyst particles. The presence of the Cu peak in EDS is due to TEM copper grid used for holding the pillared graphene sample. The high number of catalyst particles at the tips of nanotubes suggests the synthesis mechanism of CNTs to be tip-growth, which points to a low level of the interaction between substrate surface and CNTs catalyst particles. The inset selected area diffraction pattern, taken from sparsely grown CNTs area of pillared graphene, shows concentric circles. This is expected because multiwall carbon nanotubes are concentric tubes of cylindrically rolled graphene layers; therefore, we have overlapping sp^2 carbon planes of random orientation with respect to incident electron beam. Furthermore, the typical six-fold symmetry in diffraction spots supports the presence of mono- to few-layer underlying graphene film.[31, 49, 50]

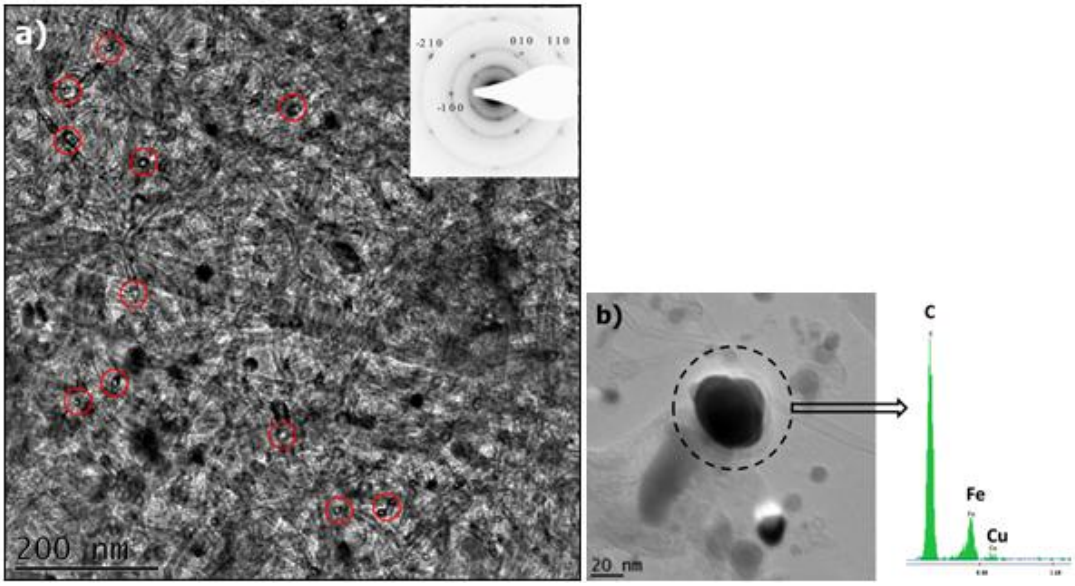

Figure 2-2-8 (a) TEM micrograph of pillared graphene bottom-view displaying CNTs roots at their interfaces with graphene film, and their tips; inset SAED diffraction

pattern taken from pillared graphene. (b) Typical EDS spectrum taken from CNTs tips (dashed circle).

We further investigate the CNT-graphene hybrid films and catalyst surfaces using Transmission Electron Microscopy (TEM; Philips, CM300) with a LaB_6 cathode operated at 300kV and equipped with an X-ray energy-dispersive spectroscopy (EDS) module. TEM samples were prepared by collecting the etched graphene-CNT films suspended on D.I. water, with a TEM copper grid. Selected area electron diffraction patterns on the graphene-CNT films change from one location to another (Figure 2-9). The main difference observed is the appearance of other sets of hexagonal spots and the amplification of the ring patterns on the locations with dense CNT growth.

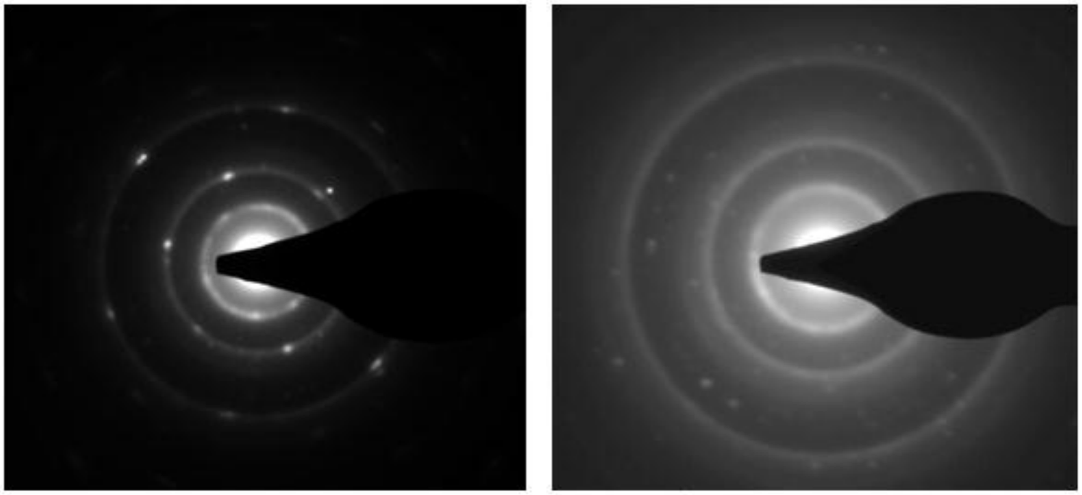

Figure 2-9 Electron diffraction patterns on the graphene/CNT films change from one location to another. Main difference observed is the appearance of other sets of hexagonal spots and the amplification of the ring patterns, on the locations with dense CNT growth.

Figure 2-10a shows TEM micrograph of bottom view of patterned PGN suspended on lacey carbon supported TEM Cu grid. The patterned PGN is clearly visible on the graphene surface. However, wrinkles and bulk defects (as shown with arrowheads) were appeared on the graphene film due to the thermal expansion coefficient mismatch between Cu and graphene, and the hollow structure of the Cu TEM grid. Figure 2-10b shows enlarged TEM micrograph of the bottom view of the PGN. This is a significant observation of the interface between CNT pillars and graphene of the PGN. The individual CNT's root is directly connected to the graphene surface. The circular hollow patterns in the interface of a CNT and graphene layer are clearly visible as shown with the dashed circles in Figure 2-10b. The inset electron diffraction pattern in Figure 2-10b consists of concentric rings which are expected since multiwalled carbon nanotubes are concentric tubes of cylindrically rolled graphene layers. The embedded typical six-fold symmetrical spots are made possible due to the mono- or bi-layer graphene film. Figure 2-10c shows HRTEM micrograph of the interface between a CNT and graphene. The clear lattice fringe on the interface confirmed seamless crystalline interface of the two carbon allotropes. The inset EDS spectrum in Figure 2-10d taken from Fe catalyst particle on the tip of a CNT (dashed circle) confirmed the existence of C, Fe and Cu elements. The Cu peak appeared due to the TEM Cu grid used for holding the PGN. TEM observations also revealed the growth mechanism of CNT pillars on the graphene layer through a vapor-liquid-solid mechanism. Our methodology provides a pathway for fabricating novel 3D nanostructures with potential applications in energy storage, photovoltaics and nanoelectronics.

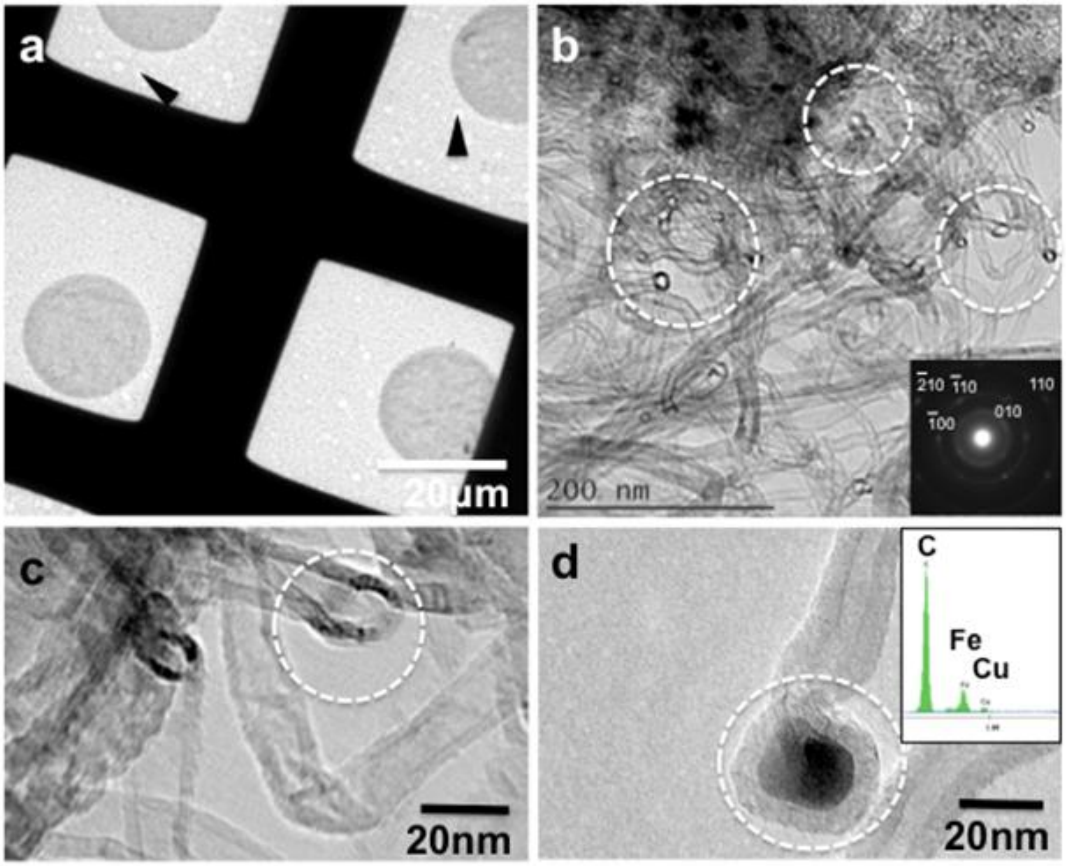

Figure 2-10(a) Low magnification TEM micrograph of micropatterned large-area PGN suspended on lacey carbon supported TEM Cu grid. (b) TEM micrograph of PGN (bottom view) showing crystalline integrity of individual CNT's root (dashed circles) with the surface of the. [36]

2.5 Demonstration of PGN based Supercapacitor Cells

To further prove the potential of the hybrid for energy storage, as-synthesized PGN were utilized as supercapacitor electrode. The supercapacitor cells were prepared from as grown PGN films as described in the experimental section. A two-electrode measurement was then employed for the electrochemical assessment, where the pre-treated two glass slides were assembled split flat cell with the as-soaked polypropylene working as a separator in between. The measurements of cyclic voltammetry (CV) were conducted to show the performance of the supercapacitor. The cyclic voltammetry scans were performed between 0 and 1 V in 6 M KOH aqueous solution (Figure 2-11 and 2-12).

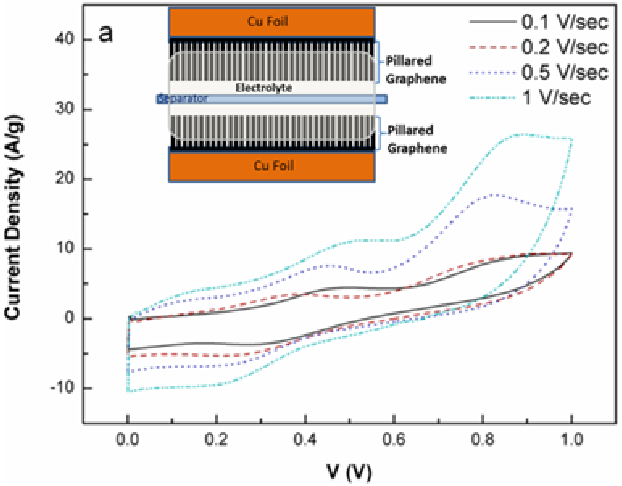

Figure 2-11 (a) CV curves of supercapacitor based on as-grown PGN films. The weight of one PGN film is around 200 μg/cm2. Electrolyte: 6 M KOH aqueous; inset: schematic of supercapaitor cell assembly.

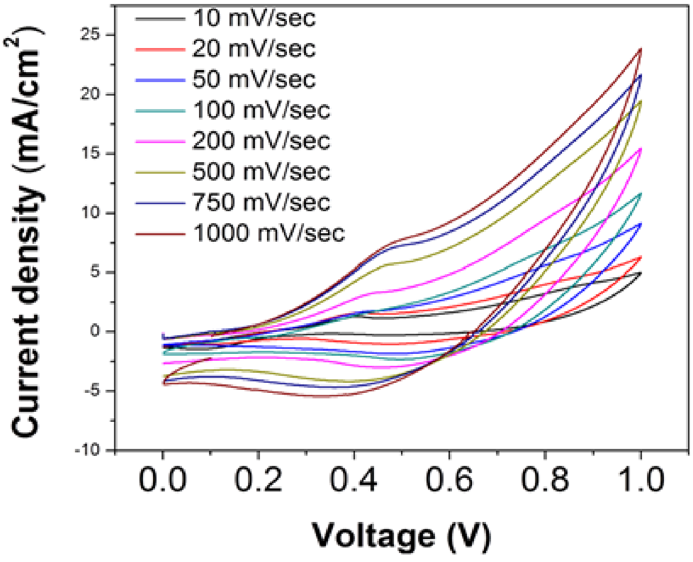

Figure 2-12 CV curves of supercapacitor based on HNO3 acid treated PGN films. The weight of one PGN film is around 200 μg/cm2. Electrolyte: 6 M KOH aqueous.

All of the C_S curves show identical behaviour. The specific capacitance can be calculated from the curve by using the Equation 1.

$$C_s = \frac{\int IdV}{m \times \Delta V \times S} \tag{1}$$

Where C_S is the specific capacitance, $\int IdV \int IdV$ is the integrated area of the CV curve, m is the mass of the active materials, ΔV is the potential range, and S is the scan rate. On the first cell (fabricated from as-grown PGN with no further treatment), the specific capacitance of 72.5 F/g, 38.15 F/g, 25.6 F/g and 18.3 F/g were obtained for the sweep rates of 0.1, 0.2, 0.5, 1 V/sec, respectively (Figure. 2-11). The distortion of CV curve from rectangular shape is due to Faradic reactions. The redox peaks around 0.4 V and 0.8V indicates the reaction between Fe catalyst and electrolyte. The relatively low specific capacitance compared with the previously reported chemically exfoliated graphene-CNT hybrid and pure graphene is due to the low surface energy of the as synthesized graphene-CNT nanostructure. Recent research has shown that activated surface of the carbon material will have higher capacitance which provides opportunity to increase the performance of the carbon-based storage devices.[52]

We repeated the measurements on samples after treatment with HNO_3 aqueous solution (HNO_3: D.I. Water=1:4). The specific capacitance of 655 F/g, 420 F/g, 154 F/g, 102 F/g, 55 F/g, 40 F/g were obtained for the sweep rates of 10, 20, 100, 200, 500, and 1000 mV/sec, respectively (Figure 2-12). Highest specific capacitance of 655 F/g, achieved at a scan rate of 10 mV/sec, suggests the as prepared supercapacitor cell has good performance. [51] Nitric acid treatment can etch Fe catalyst and oxides away, and at the same time enhances the surface wettability of the carbon hybrid. Therefore, the surface area increases by means of end-tip opening of carbon nanotubes, which further increases the specific capacitance (Figures 2-12 and 2-13). The energy density was calculated by using Equation 2.

$$E = \frac{1}{2} C_s \left(\Delta V \right)^2 \tag{2}$$

The energy density increases from 10.05 to 91 Wh/kg (for 10 mV/sec) after acid treatment, demonstrating a good performance of the Pillared Graphene Nanostructure supercapcitor comparable to those of carbon based supercapacitors.[53, 54]

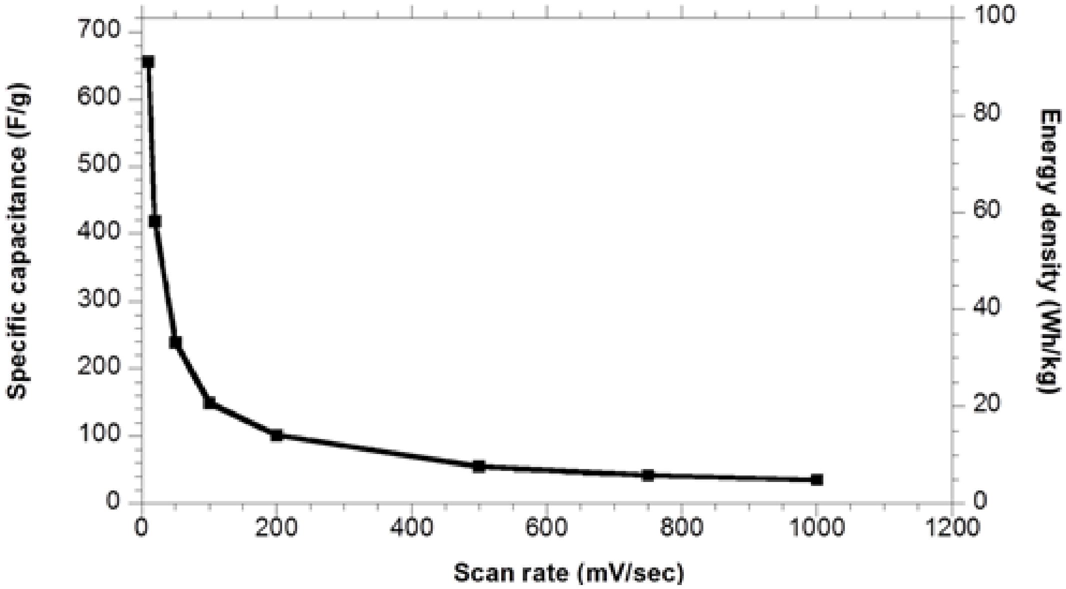

Figure 2-2-13 Specific capacitance and energy density vs. scan rates

2.6 Conclusion

Large and uniform pillared graphene films were successfully synthesized via simultaneous CVD growth of graphene layers and carbon nanotubes on copper foil. The introduced graphene-CNT hybrid is a remarkable carbon nanostructure with tuneable nano-architectonics, which is central to application-oriented design of hierarchical graphene structures. The unique mechanism of synchronized CVD growth of CNT and graphene contributed significantly to the composure of the final carbon structure. Detailed characterization of synthesized pillared graphene shows the cohesive structure and crystalline contact between the two carbon allotropes in the hybrid. Through its tuneable spatial geometry and attractive material properties, this carbon hybrid shows very promising potential for integration into nanoelectronics, energy storage, and thermal management. These attractive material properties stem from the fact that the synthesized pillared graphene is exclusively built from sp^2 hybridized carbon atoms. The direct growth of PGN on copper foil, a significant technical improvement, opens the door for realistic applications of PGN, in which it is necessary to have a mechanically flexible and electrically/thermally conductive substrate. As an immediate proof for the functionality of the refined graphene hybrid structure, it has been readily implemented into a supercapacitor cell. The measurement of the supercapacitor cell demonstrates relatively high energy density with good cycling stability that paves the way for developing future higher energy storage devices.

The present work is also innovative for its synchronous approach to synthesis of multi-component hybrids. The introduced fabrication methodology is based on premeditated design of catalysts foundation, analysis of carbon formation mechanisms, and thoughtful timing in the fabrication procedure, as synchronization in the growth process is vital. Accordingly, chemical nature, morphology, and organization of the catalysts, as well as pre-processing of the growth substrate, are the key designing measures of this methodology. The synchronous parallel growth methodology offers an ideal mass production technique for carbon hybrids. It also does not involve any unconventional laboratory-style step, and is highly compatible with industrial thin-film fabrication technologies.

2.7 References

1. K. S. Novoselov, A. K. Geim, S. V. Morozov, D. Jiang, M. I. Katsnelson, I. V. Grigorieva, S. V. Dubonos and A. A. Firsov, *Nature*, 2005, **438**, 197-200.
2. K. S. Novoselov, A. K. Geim, S. V. Morozov, D. Jiang, Y. Zhang, S. V. Dubonos, I. V. Grigorieva and A. A. Firsov, *Science*, 2004, **306**, 666-669.
3. Y. Zhang, Y.-W. Tan, H. L. Stormer and P. Kim, *Nature*, 2005, **438**, 201-204.
4. A. K. Geim and K. S. Novoselov, *Nat. Mater.*, 2007, **6**, 183-191.
5. J.-H. Chen, C. Jang, S. Xiao, M. Ishigami and M. S. Fuhrer, *Nat Nano*, 2008, **3**, 206-209.
6. A. A. Balandin, S. Ghosh, W. Bao, I. Calizo, D. Teweldebrhan, F. Miao and C. N. Lau, *Nano Lett.*, 2008, **8**, 902-907.

7. C. Lee, X. Wei, J. W. Kysar and J. Hone, *Science*, 2008, **321**, 385-388.

8. F. Schedin, A. K. Geim, S. V. Morozov, E. W. Hill, P. Blake, M. I. Katsnelson and K. S. Novoselov, *Nat. Mater.*, 2007, **6**, 652-655.

9. X. Wang, L. Zhi and K. Mullen, *Nano Lett.*, 2007, **8**, 323-327.

10. J. Yan, T. Wei, B. Shao, Z. Fan, W. Qian, M. Zhang and F. Wei, *Carbon*, 2009, **48**, 487-493.

11. J. Lin, D. Teweldebrhan, K. Ashraf, G. Liu, X. Jing, Z. Yan, R. Li, M. Ozkan, R. K. Lake, A. A. Balandin and C. S. Ozkan, *Small*, 2010, **6**, 1150-1155.

12. E. Yoo, J. Kim, E. Hosono, H.-s. Zhou, T. Kudo and I. Honma, *Nano Lett.*, 2008, **8**, 2277-2282.

13. S. Iijima, *Nature*, 1991, **354**, 56-58.

14. M. S. Dresselhaus, G. Dresselhaus and A. Jorio, *Annual Review of Materials*, 2004, **34**, 247-278.

15. Popov and N. Valentin, *Materials Science and Engineering*, 2004, **43**, 42.

16. P. G. Collins, M. S. Arnold and P. Avouris, *Science*, 2001, **292**, 706-709.

17. A. Javey, J. Guo, Q. Wang, M. Lundstrom and H. Dai, *Nature*, 2003, **424**, 654-657.

18. W. A. de Heer, A. Chatelain and D. Ugarte, *Science*, 1995, **270**, 1179-1180.

19. D. H. Lee, J. E. Kim, T. H. Han, J. W. Hwang, S. Jeon, S.-Y. Choi, S. H. Hong, W. J. Lee, R. S. Ruoff and S. O. Kim, *Adv. Mater. (Weinheim, Ger.)*, 2010, **22**, 1247-1252.

20. H. Y. Jeong, D.-S. Lee, H. K. Choi, D. H. Lee, J.-E. Kim, J. Y. Lee, W. J. Lee, S. O. Kim and S.-Y. Choi, *Appl. Phys. Lett.*, 2010, **96**, 213105-213103.

21. D. Yu and L. Dai, *The Journal of Physical Chemistry Letters*, 2009, **1**, 467-470.

22. V. C. Tung, L.-M. Chen, M. J. Allen, J. K. Wassei, K. Nelson, R. B. Kaner and Y. Yang, *Nano Lett.*, 2009, **9**, 1949-1955.

23. G. K. Dimitrakakis, E. Tylianakis and G. E. Froudakis, *Nano Lett.*, 2008, **8**, 3166-3170.

24. M. D. Stoller, S. Park, Y. Zhu, J. An and R. S. Ruoff, *Nano Lett.*, 2008, **8**, 3498-3502.

25. D. H. Lee, J. A. Lee, W. J. Lee, D. S. Choi, W. J. Lee and S. O. Kim, *The Journal of Physical Chemistry C*, 2010, **114**, 21184-21189.

26. D. H. Lee, J. A. Lee, W. J. Lee and S. O. Kim, *Small*, 2011, **7**, 95-100.

27. C. Gomez-Navarro, J. C. Meyer, R. S. Sundaram, A. Chuvilin, S. Kurasch, M. Burghard, K. Kern and U. Kaiser, *Nano Lett.*, 2010, **10**, 1144-1148.

28. Z. Fan, J. Yan, L. Zhi, Q. Zhang, T. Wei, J. Feng, M. Zhang, W. Qian and F. Wei, *Adv. Mater. (Weinheim, Ger.)*, 2010, **22**, 3723-3728.

29. P. Blake, P. D. Brimicombe, R. R. Nair, T. J. Booth, D. Jiang, F. Schedin, L. A. Ponomarenko, S. V. Morozov, H. F. Gleeson, E. W. Hill, A. K. Geim and K. S. Novoselov, *Nano Lett.*, 2008, **8**, 1704-1708.

30. L. A. Ponomarenko, F. Schedin, M. I. Katsnelson, R. Yang, E. W. Hill, K. S. Novoselov and A. K. Geim, *Science*, 2008, **320**, 356-358.

31. A. Reina, X. Jia, J. Ho, D. Nezich, H. Son, V. Bulovic, M. S. Dresselhaus and J. Kong, *Nano Lett.*, 2008, **9**, 30-35.

32. K. S. Kim, Y. Zhao, H. Jang, S. Y. Lee, J. M. Kim, K. S. Kim, J.-H. Ahn, P. Kim, J.-Y. Choi and B. H. Hong, *Nature*, 2009, **457**, 706-710.

33. X. Li, W. Cai, J. An, S. Kim, J. Nah, D. Yang, R. Piner, A. Velamakanni, I. Jung, E. Tutuc, S. K. Banerjee, L. Colombo and R. S. Ruoff, *Science*, 2009, **324**, 1312-1314.

34. M. P. Levendorf, C. S. Ruiz-Vargas, S. Garg and J. Park, *Nano Lett.*, 2009, **9**, 4479-4483.

35. X. Dong, B. Li, A. Wei, X. Cao, M. B. Chan-Park, H. Zhang, L.-J. Li, W. Huang and P. Chen, *Carbon*, 2011, **49**, 2944-2949.

36. R. K. Paul, M. Ghazinejad, M. Penchev, J. Lin, M. Ozkan and C. S. Ozkan, *Small*, 2010, **6**, 2309-2313.

37. I. Lahiri, R. Seelaboyina, J. Y. Hwang, R. Banerjee and W. Choi, *Carbon*, 2010, **48**, 1531-1538.

38. G. Li, S. Chakrabarti, M. Schulz and V. Shanov, *Journal of Materials Reseach*, 2009, **24**, 2813-2820.

39. H. Wang, J. Feng, X. Hu and K. M. Ng, *The Journal of Physical Chemistry C*, 2007, **111**, 12617-12624.

40. L. Delzeit, C. V. Nguyen, B. Chen, R. Stevens, A. Cassell, J. Han and M. Meyyappan, *The Journal of Physical Chemistry B*, 2002, **106**, 5629-5635.

41. J. J. De Yoreo and P. G. Vekilov, *Rev. Mineral. Geochem.*, 2003, **54**, 57-93.

42. D. R. Askeland and P. P. Phule, *The Science and Engineering Of Materials* Thomson Learning, 2005.

43. Z. L. Wang, Y. Liu and Z. Z. Kluwer, *Handbook of Nanophase and Nanostructured Materials*, Academic/Plenum Publishers, 2002.

44. C. P. Wang, X. J. Liu, M. Jiang, I. Ohnuma, R. Kainuma and K. Ishida, *J. Phys. Chem. Solids*, 2005, **66**, 256-260.

45. M. Haluska, M. Hirscher, M. Becher, U. Dettlaff-Weglikowska, X. Chen and S. Roth, *Materials Science and Engineering B*, 2004, **108**, 130-133.

46. H. J. Park, J. Meyer, S. Roth and V. Skákalová, *Carbon*, 2010, **48**, 1088-1094.

47. R. T. K. Baker, *Carbon*, 1989, **27**, 315-323.

48. A. M. Cassell, J. A. Raymakers, J. Kong and H. Dai, *The Journal of Physical Chemistry B*, 1999, **103**, 6484-6492.

49. J. C. Meyer, A. K. Geim, M. I. Katsnelson, K. S. Novoselov, T. J. Booth and S. Roth, *Nature*, 2007, **446**, 60-63.

50. J. C. Meyer, A. K. Geim, M. I. Katsnelson, K. S. Novoselov, D. Obergfell, S. Roth, C. Girit and A. Zettl, *Solid State Commun.*, 2007, **143**, 101-109.

51. D. N. Futaba, K. Hata, T. Yamada, T. Hiraoka, Y. Hayamizu, Y. Kakudate, O. Tanaike, H. Hatori, M. Yumura and S. Iijima, *Nat. Mater.*, 2006, **5**, 987-994.

52. Y. Zhu, S. Murali, M. D. Stoller, K. J. Ganesh, W. Cai, P. J. Ferreira, A. Pirkle, R. M. Wallace, K. A. Cychosz, M. Thommes, D. Su, E. A. Stach and R. S. Ruoff, *Science*, 2011, **332**, 1537-1541.

53. A. Yu, I. Roes, A. Davies and Z. Chen, *Appl. Phys. Lett.*, 2010, **96**, 253105.

54. L. Hu, J. W. Choi, Y. Yang, S. Jeong, F. La Mantia, L.-F. Cui and Y. Cui, *Proceedings of the National Academy of Sciences*, 2009, **106**, 21490-21494.

Chapter 3

3. Block Copolymers Patterning of Catalysts Arrays for CVD Growth of Carbon Nanostructures

3.1 Introduction

Block Copolymers are a class of self-assembly polymers that are composed of two or more chemically different polymer segments or blocks.[1-5] The polymer blocks in BCP macromolecule are covalently attached in well-defined sequences. In the most basic case, BCPs are derived from two linearly linked segments (here labeled as block X and Y), and is referred to as X-b-Y dibock copolymers. For example, the copolymer polystyrene-b-poly (methyl methacrylate), abbreviated as PS-b-PMMA, is made up monomers of polystyrene that are covalently bonded to poly (methyl methacrylate). The block copolymers that are derived from three and more monomers are termed as triblock and multiblock copolymers, respectively. [1-5]

Block copolymers can be synthesized by different living polymerization techniques, in which the end of copolymer chain is kept active after each addition of each monomer block.[1-5] As a result, monomer blocks could be added step by step to the synthesized copolymer chain in polymerization process.

The distinctive feature of block copolymers (BCPs) is their ability to phase separate on micro/nano-scale, which is called microphase separation. Owing to this capability, BCPs can form periodic and well organized nano-scale patterns and structures. The nature of micro-phase separation is essentially very similar to visible macro-scale separation of immiscible liquids such as oil and water. In the BCP microphase separation, however, due to the covalent bonding between different polymer blocks they cannot macroscopically separate. The covalent attachment, combined with incompatibility of the blocks, result in "local" nanometer-sized separation of the polymer blocks, allowing BCPs to self-assemble into a verity of interesting and complex shapes. The final morphology of a BCP mainly depends on relative length, chemical nature, and molecular weight of the constituent blocks. Since we intend to implement diblock copolymers, we primarily focus on the self-assembly morphologies that are developed by micro-phase separation of two polymer blocks. [1-5]

In diblock copolymers, the final shape and microphase separation is primarily determined by the ratio between the volume of each block, the total number of monomers in BCP (polymerization degree), and the incompatibility of the two building polymer blocks. The latter factor is called Flory-Huggins interaction parameter, χ (chi), that basically show how much two polymer blocks dislike each other.[1-5] Another factor involved in phase behavior of block copolymer is the relative volume fraction that each block occupies in the entire body of BCP structure. Based on this fraction, the thermodynamic propensity to minimize the interfacial surface area, determines the resulting morphologies in diblock copolymers. [1-5] Similar values for volume fraction of the two blocks, around 0.5 for each blocks, result in layered polymer morphology that is called lamellar structure.[1,6,7] Upsetting the minor volume fraction to around 0.2 and 0.3, results in spherical[1,8] and cylindrical [1, 9-15] morphologies of minor blocks in the matrix of major polymer. Other complex morphologies, like gyroidal structures at around 0.38 volume fraction, are also possible.[1-5] In addition to the adaptable morphologies, desired functionality could be integrated to diblock copolymers by premeditated selection of constituent blocks with specific chemical functional groups. With their versatility in shape, size, spacing, and chemical functionality, diblock copolymers are highly effective materials for fabrication and patterning of functional nanostructures. [1-5, 9-17]

For design and construction of the desired carbon structure, like any other structures, it's necessary to first build the foundation. In our case the foundation consists of nano-scale metal dots (catalyst seeds) upon which the whole graphene structure is built up. These metal nanoparticles are applied as catalysts for the growth of carbon structures, and therefore, are the base of the final carbon architecture. The interest here lies in producing and patterning arrays of catalyst particles with controlled size and separation distance which result in controlled diameter and separation distance of grown carbon nanotubes, and eventually controlled amount of final surface area (the key parameter). In other words, the more organized and uniform metallic seeds are the more efficient and controllable our final graphene structure and its surface area will be.

Based on the targeted ordering and distribution, we primarily focused on hexagonal arranged cylindrical diblock copolymers. This dictates the volume fraction to be around 0.3 for the minor block in 0.7 of major block.[1-5, 9-15] Due to desired chemical functionality of polyvinylpyridine family (PnVP), we selected the diblock copolymer of polystyrene and polyvinylpyridine (PS-b-PnVP) as our main construction materials. We will discuss our choice more in details later in this chapter.

3.2 Casting and Alignment of Cylindrical Block Copolymer

Here we focus on the experimental procedure of casting and alignment of cylindrical block copolymer, which is a requirement for achieving large-scale patterned arrays of catalyst particles. Polystyrene-b-Polyvinylpyridine (PS-b-PnVP) BCPs with a polydispersity below 1.15 and PnVP volume fraction of 0.3 are purchased from Polymer Source Inc., as the raw material for this study. Due to the selected volume fraction the copolymer microphase assemble into cylindrical nano-domains with hexagonal lattice arrangement. As mentioned before, the periodicity and the separation distance are controlled by the molecular weight of polymer blocks. Therefore, to obtain cylinders of smaller diameter and spacing one should synthesize polymer blocks of shorter chain (smaller molecular weight) during the polymerization procedure. [1, 9-13]

Typically, when a non-selective solution of block copolymer is spin coated on top of a flat substrate, because of the interactions between the blocks and the substrate, polymer domains would organize parallel to the substrate.[1-7,9-15] This natural self-organization of the copolymers, for reaching thermodynamic equilibrium, leads to random planer arrangement which obviously is not desired. Below is the example of the result that we got from our first casting attempts. As it can be seen, cylindrical P2VP are randomly oriented in the matrix PS.

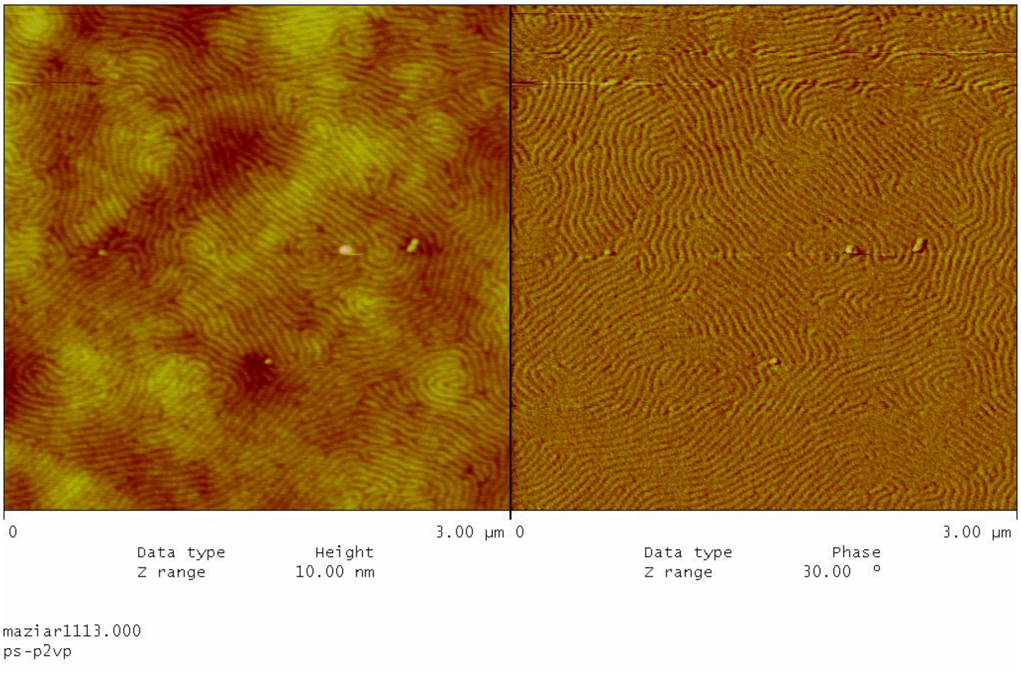

Figure 3-1 AFM image of the spin coated PS-b-PVP film with cylindrical nano-domains parallel to the substrate

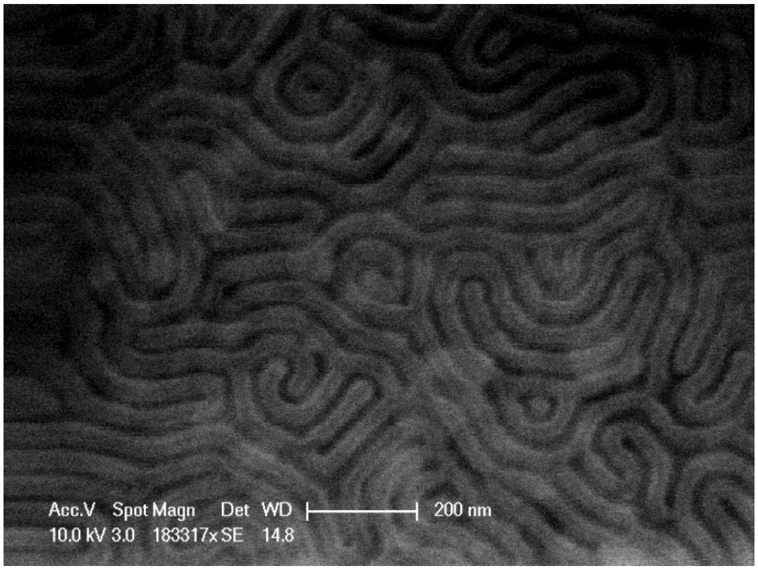

Figure 3-2 SEM image of the spin coated cylindrical PS-b-P4VP diblock copolymer film

In order to achieve vertical alignment of cylindrical domains different strategies, depending on the chemical and physical nature of the used polymers, are applied. In the context of pattering catalyst arrays, we focused our attempts on a solvent annealing alignment of BCP films that has been recently introduced and applied by Russell's group in University of Massachusetts. [9-15] Solvent annealing involves exposure of BCP polymer domains to a controlled and constant solvent vapor, which interact with different polymer blocks and redefine their long range ordering and orientation. Evaporation of solvent is generating a directional and selective chemical environment which penetrates into BCP thin layer and reorients the minor blocks domains in the major polymer matrix. This technique, among other block copolymers, can be used to align the cylinder domains of PS-b-PnVP vertical to the substrate.[9-13] For example in the case of P(S-4VP), after block copolymer solution is spin coated on the substrate, its films are vapor annealed in a saturated toluene/THF (1/4, volume ratio) environment. In our initial attempts of solvent annealing we gained some mixed vertical alignment. The quality of the initial cylindrical BCPs were not satisfactory for the next step which was the catalyst deposition and patterning. After several trial and errors and customizing the experiment parameters we managed to achieve full vertical alignment in cylindrical domains. Figures 3-4 and 3-5 show the vertical alignment of cylindrical nano-domains via solvent annealing. This technique is most applicable for PS-PnVP BCPs, which are of crucial importance in our research because of their chemical nature. The time progress of solvent annealing is shown in the following AFM images (Figure 3-3).

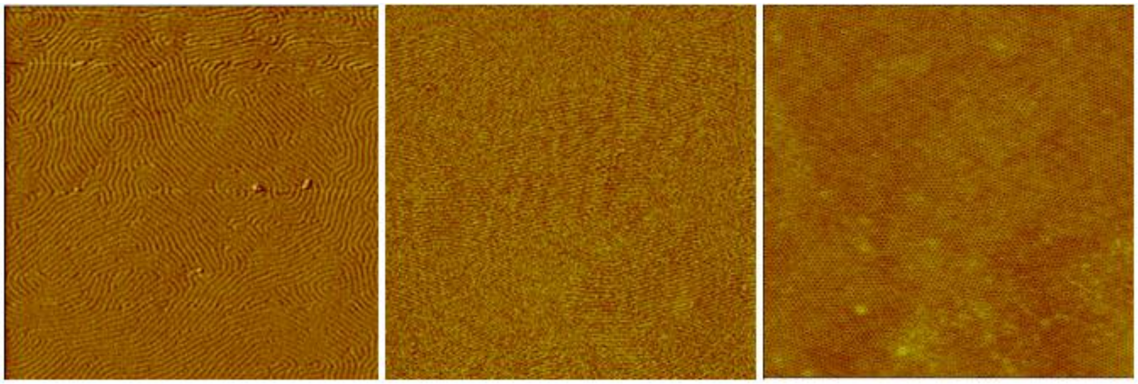

Figure 3-3 AFM images of cylindrical PS-P4VP. From left to right: as spin coated (before solvent annealing), after 30 minutes exposure to THF vapor (during solvent annealing), and vertically aligned P4VP domains upon completion of solvent annealing

Another important element which should be considered in the hexagonally organized diblock copolymers is the effect of molecular weight. Figure 3-4 shows AFM images of solvent annealed cylindrical PS-P4VP with molecular weight of 166

Kg/mol, 69 Kg/mol, and 32 Kg/mol. It can be easily observed that as the molecular weight increases the size (diameter) and separation distances of the cylindrical domains increase.

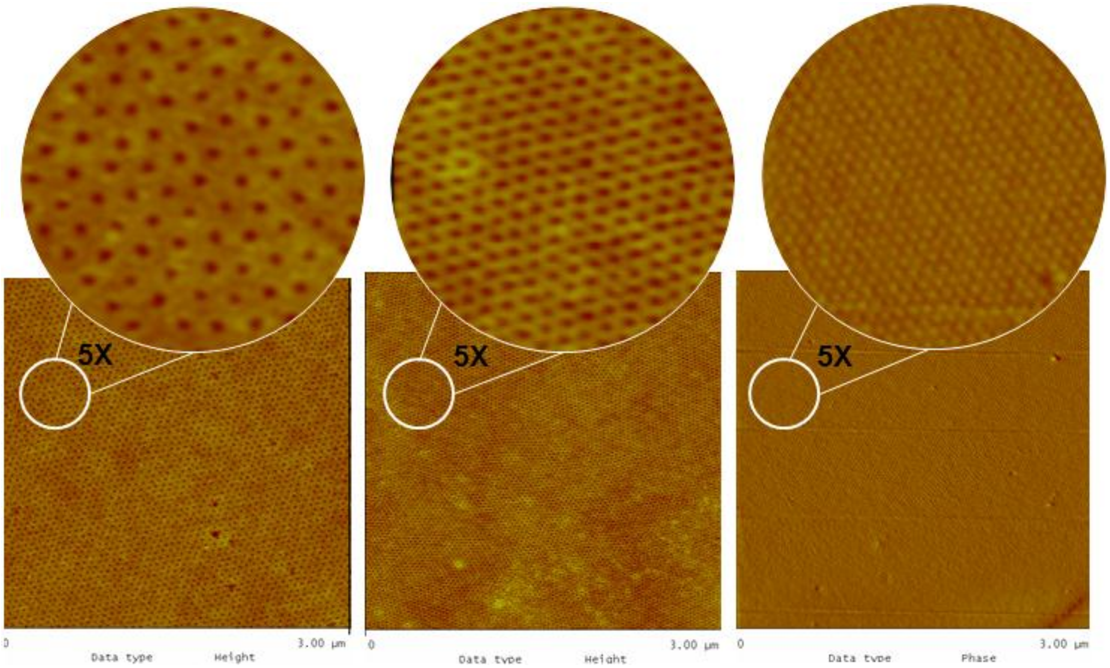

Figure 3-4 AFM images of cylindrical PS-P4VP aligned vertically to the substrate. From left to right: molecular weight is 166 Kg/mol , 69 Kg/mol, and 32 Kg/mol

3.3 Block Copolymers as Catalyst templates for Chemical Vapor Deposition of Nano-fabrics

In order to use carbon nanotube and nanowires in realistic energy and electronic devices we need well-aligned large-scale arrays of these nanostructures on suitable substrates. As a vital part of in situ fabricating of parallel arrays of nanowires, it is necessary to develop a method for fabricating and patterning arrays of catalyst nanoparticles. The catalyst particles are used as seeds for growing nanowires through chemical vapor deposition, and therefore, are considered as the cornerstone of desired nanostructures. The interest here lies in fabrication of arrays of catalyst particles with controlled size and spacing on top of the growth substrate. For this purpose, we implemented solvent annealing method to achieve hexagonal lateral distribution, as described in previous section. Later in this chapter we discuss hybrid approaches that combine top-down methods with self-assembly of cylindrical block copolymer.

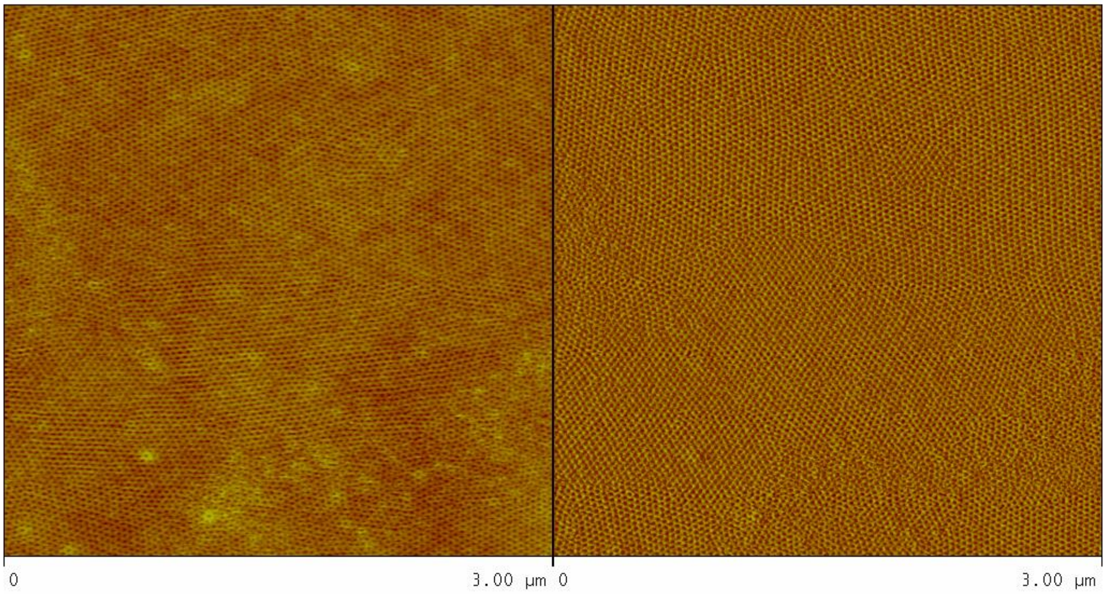

Figure 3- Vertical alignment of nano-domains in cylindrical diblock copolymers; dark dots represent hexagonally ordered cylindrical domains (minor component) and lighter background shows the matrix (major component)

After vertical alignment of BCP nano-domains by solvent annealing method described in previous section, they are chemically loaded with desired metallic catalyst ions. The choice of metallic ion depends on the target structure-function of the nano-fabric that is to be synthesized by use of the resulting catalyst metal arrays. Some typical choices include Au^{+3}, Fe^{+3}, Cu^{+2}, and Co^{+2}. [9-13, 16-18] In general, the chemical nature of the minor block which achieved through proper selection of constituent polymers, guarantees selective absorption of the catalytic ions to cylinders and not to the matrix (major block) in BCP film. [1, 9-13, 16-18]

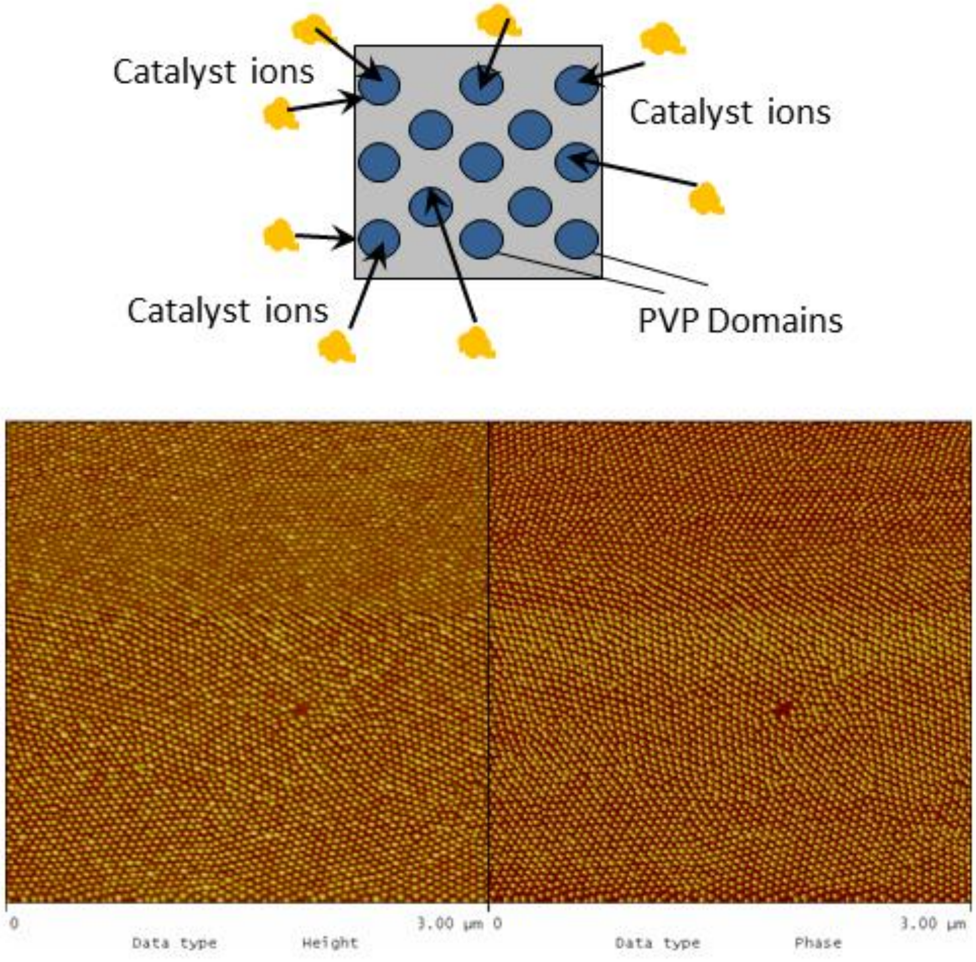

Figure 3-5 Schematic and AFM image of selective incorporation of catalyst ions to cylindrical domains of PS-b-P4VP due to chemical nature of P4VP cylinders.

After completion of the loading step, different techniques can be used to chemically reduce the metallic ions into zero-valent metal nanoparticles in the BCP cylindrical nano-domains, and remove the remaining BCP template. In chemical methods, reduction is done by use of reducing agents, like hydrazine N_2H_4. In physical method, dry exposure techniques, including irradiation with electron beam, ultraviolet light, or plasma treatment are applied to chemically reduce the catalyst ions and remove the BCP film. Typically dry techniques produce more uniform and consistent catalyst arrays, and remove polymer template more effectively. Figure 3-5 shows AFM image of 69K PS-b-P4VP after solvent annealing and before loading of metallic ions. Subsequently, the solvent annealed BCP film is dipped in 1 wt.% $HAuCl_4$, for incorporation of Au^{+3} ions into P4VP domains. The Au^{+3} loaded BCP is then treated with Oxygen plasma by reactive ion etching to reduce gold ions and remove polymer film, resulting in nano-scale ordered arrays of hexagonally packed gold nano particles (Figure 3-6). When compared with conventional techniques for deposition of catalyst particles for CVD growth, diblock copolymer fabricated catalyst arrays show a clear superiority in terms of uniformity of size, morphology and distribution of catalyst particles (Figure 3-7).

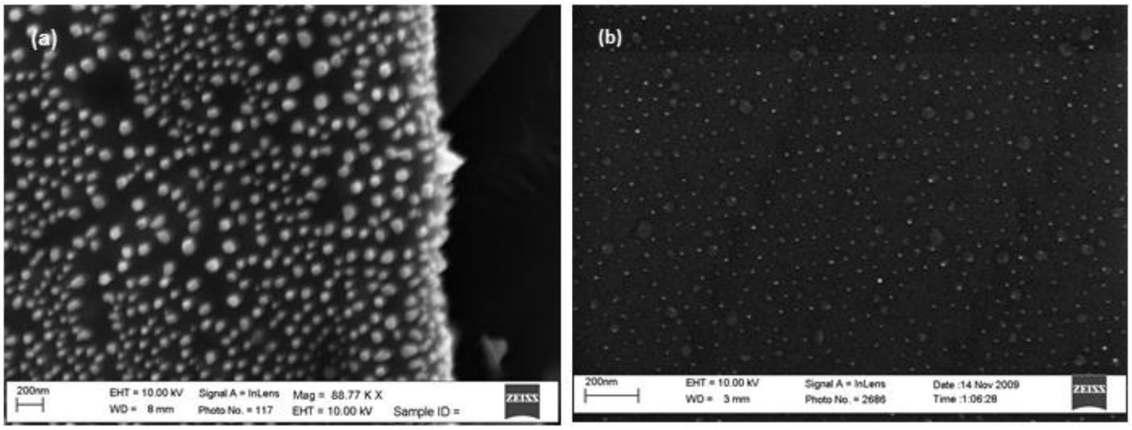

Figure 3-6 SEM images of: (a) gold particles randomly deposited by e-beam evaporation (mainstream method), and (b) the gold catalyst arrays fabricated by block copolymer template (right); block copolymer strategy clearly shows superiority in terms of uniformity of size, morphology and distribution of catalyst particles

3.4 Tuning the Architecture of Hybrid Carbon nanostructures with Block Copolymer Self-assembly

In this section we study block polymer assisted CVD growth of carbon nanostructures. To utilize the capabilities of pillared graphene for energy storage a well-thought-out architectonic design needs to be devised and executed. As we discussed, the foundation of this architecture consists of nano-sized metallic particles (catalyst seeds) upon which the whole carbon nanostructure is built up (Figures 3-7 and 3-8). These catalyst metal dots are utilized as the catalyst foundation for the growth of carbon nanotube pillars in graphene – CNT structures.

Diblock copolymer utilized for generating catalysts templates is Poly (styrene-b-4-vinylpyridne) (PS-b-P4VP) with a molecular weight of 59kg/mol (M_n,PS = 47.6 kg/mol, M_n,PVP = 20.9 kg/mol) and molecular weight distribution of M_w/M_n = 1.14 (purchased form Polymer Source Inc.). The block copolymers are dissolved in a toluene/tetrahydrofuran solvent to make 0.5 wt% polymer solution that was subsequently spin-coated at 2500 rpm onto silicon wafer with 300nm thermally grown silicon dioxide on it. The as-spun copolymer films are then exposed to tetrahydrofuran vapor for 3 hours at room temperature for solvent annealing. This re-organizes the orientation of the copolymer macromolecules and yields highly aligned microstructures with larger ranges of ordering.

Upon alignment of BCP micro domains by solvent annealing, copolymer film is loaded with Iron ions through dipping in the ethanol solution of Iron salt ($FeCl_3$). This results in selective incorporation of Iron ions onto Poly (4-vinylpyridne) block. The chemical nature of minor block, Poly (4-vinylpyridne), which achieved through proper selection of polymer blocks, guarantees selective absorption of the catalytic ions to cylinders and not to the matrix (major block) in BCP film. [9-13, 16-18] Due to the fact that transition metals such as Fe, Co, Ni, Ag, Au, Pt, and Pd, have partially filled d orbitals, they form coordination bond with electron-rich ligands such as nitrogen functional group in pyridine [9-13, 16-18].

The metal loaded copolymer films are then floated off from the substrate using 1wt% HF solution and transferred to Cu foils, which has gone under a specific plasma treatment, to function as CNT seeds for growing PGN. Finally the copolymer film undergoes hydrogen annealing at 400 °C or 1 hour to remove polymer residues and reduce iron ions to metallic iron.

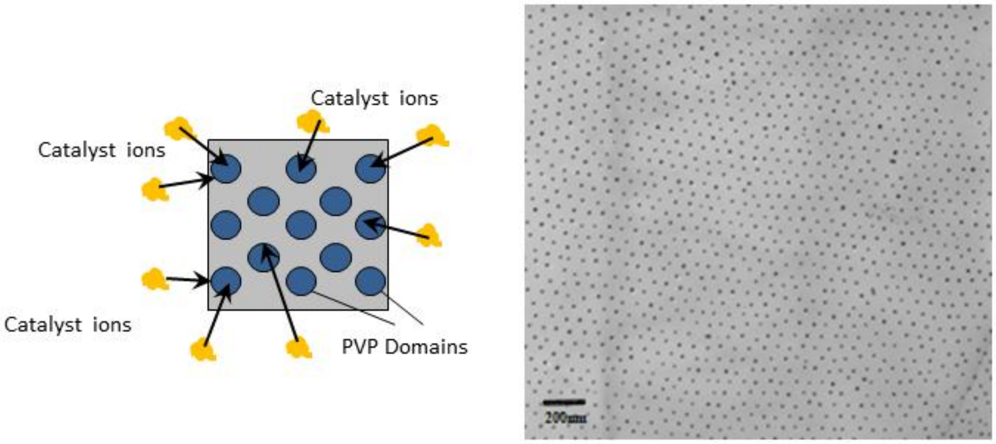

Figure 3-7 (a) Schematic and (b) TEM image of selective incorporation of Fe catalyst ions into cylindrical BCP domains due to chemical nature of minor block (cylinders)

Subsequently, the CVD reactor tube is loaded with the growth substrate (copper foil with arrays of BCP-patterned iron particles) and heated to 750°C under 300 sccm of Ar and 400 sccm of H_2 at atmosphere pressure. Once the temperature is stabilized at 750°C (after 5 minutes), 50 sccm of C_2H_2 is introduced into the tube for 20 to 30 min to initiate the synthesis of PGN. Figure 3-9 show the time progress of the CVD growth of carbon nanotubes from a BCP patterned Fe catalyst particle.

After completion of the synthesis, the feed of C_2H_2 flow is stopped and furnace is cooled to the 400°C at the rate 60°C/min and under the protection of hydrogen flow. On next step PGN layer is removed from the Cu film by etching in a 1M aqueous $FeCl_3$ solution, followed by subsequent cleaning with an aqueous HCl (5%) and D.I. water solution. PGN layer is then collected by a desired substrate (quartz or SiO_2/Si) from D.I. water solution.

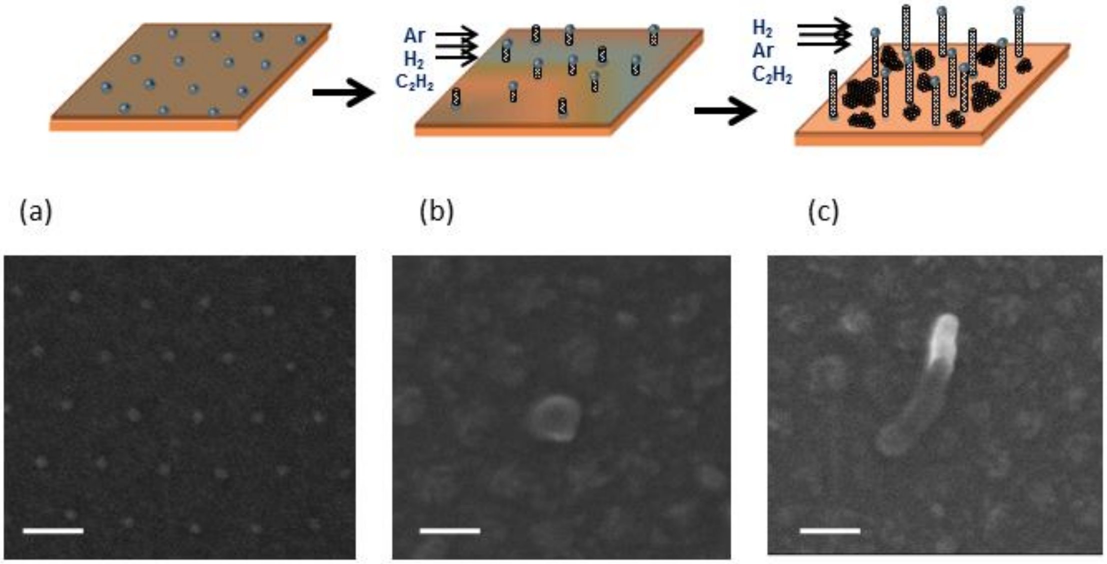

Figure 3-8 Schematic and SEM images of the different stages of the growth of carbon nanotube from BCP patterned catalyst particles; (a) BCP patterned arrays of hexagonally packed Fe nanoparticles; (b) diffusion of carbon into Fe catalyst particles (c) growth of carbon nanotube from patterned Fe catalyst particles. All scale-bars show 40 nm.

It should be noted the size and separation distance of the cylindrical micro domains in BCP templates depend on the molecular weight of the selected BCP. Figure 3-11 show Fe nanoparticles that are fabricated by PS-b-P4VP with 32 Kg/mol and 166 Kg/mol molecular weight. The size of the nanoparticles prepared from 166 Kg/mol PS-b-P4VP is around 9-10 nm, which is nearly double the size of Fe nano particles fabricated by by PS-b-P4VP with 32 Kg/mol molecular weight.

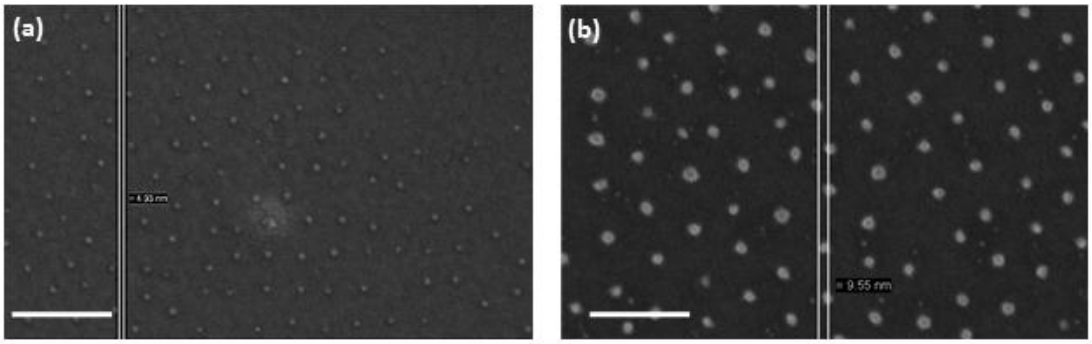

Figure 3-9 SEM images of (a) metallic nanoparticles that are fabricated by PS-b-P4VP with 32 Kg/mol and (b) 166 Kg/mol molecular weight. All scale-bars show 100 nm. Size and spacing of the BCP fabricated catalyst particles can be adjusted via the molecular weight of the selected diblock copolymer template.

This versatility in the size of BCP fabricated catalyst particles will be directly translated into the size of carbon nanotubes, which are grown from these catalyst arrays by chemical vapor deposition (Figure 3-11).

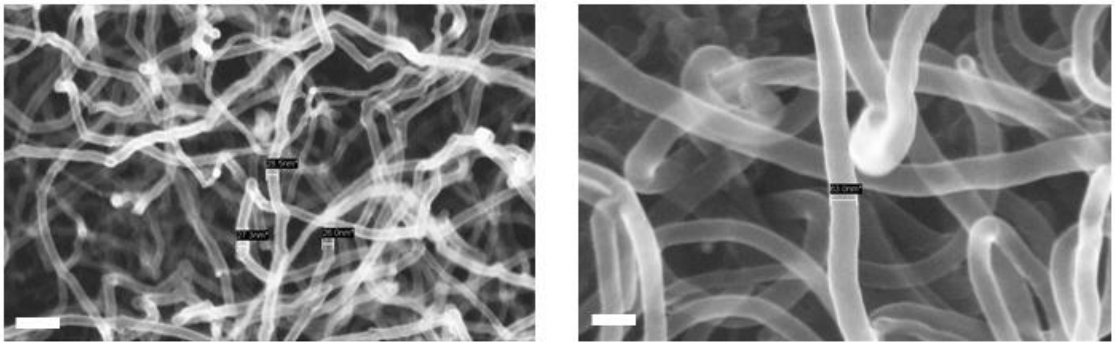

Figure 3-10 The size and molecular weight of BCP templates for catalyst particles will directly influence the size of CVD grown carbon nanotubes. All scale-bars show 100 nm

Finally figure 3-12 show the Fe catalyst particles fabricated by 69 Kg/mol PS-b-P4VP, and the carbon nanotubes that are CVD grown from these Fe catalyst arrays. As it can be seen, the resulting CNTs are dense, uniformly sized, and grown directionally.

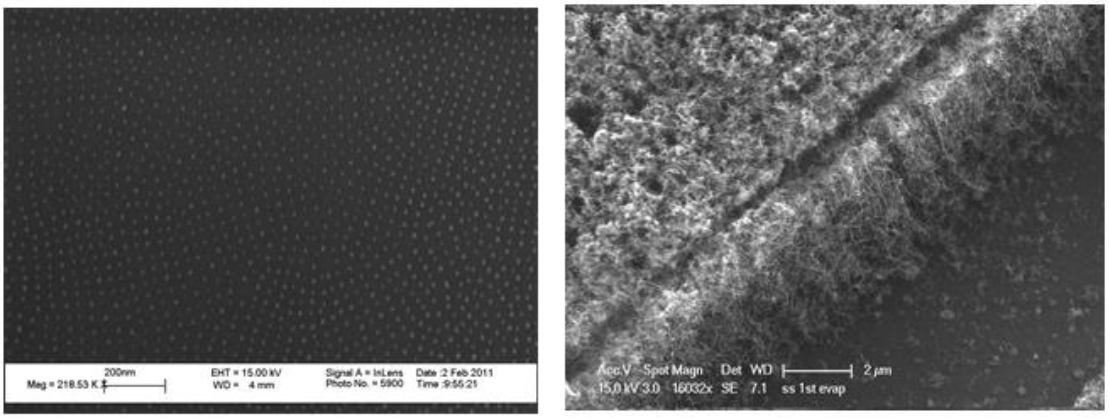

Figure 3-11 SEM images of: (a) Fe catalyst particles patterned by PS-b-P4VP block copolymer template; (b) CVD synthesized Carbon Nanotubes that used the Iron particles of image (a) as growth seeds.

3.5 Development of BCP Films on Topographically Patterned Substrates

Lithography patterned self-assembly, a combination of bottom-up with top-down strategies, provides a practical approach to achieve complex nanoscale features and bridge the gap between the manufacturing scopes of the conventional top-down nanofabrication methods and self-assembly techniques. [16-18] Such hybrid self-assembly techniques typically involve use of lithography techniques, ranging from e-beam lithography to nanoimpring lithography for topographically patterning of the substrate. Consequently, catalyst loaded diblock copolymers are coated on top these topographically altered substrates, where they are trapped in the generated patterns(Figure 3-13). BCP nano-domains are used as career for metalic catalyst ions, and their self-assembly ability is being utilized to order them within the range of the topographical patterens. As before, the morphology and size of catalyst particles can be controlled by volume fraction and molecular weight of diblock copolymer film.

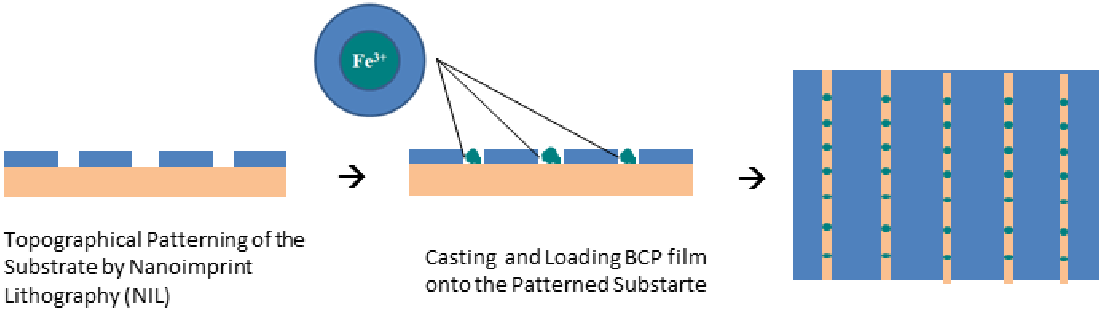

Figure 3-12 Schematic of the process in which BCP cylinders are developed on Nano-Imprint Lithography (NIL)-fabricated topographical template for pattern-assisted self-assembly of catalyst particles

For topographical patterning of the substrate we employed nanoimprint lithography (NIL) to develop trenches of uniform width and separation distance on top of the substrate. PS-b-PVP polymer solution is spin coated on top of this patterned substrate and then loaded with Fe catalyst ions. Figure 3-14 shows AFM image of NIL patterned substrate that is coated with PS-b-PVP diblock copolymer film. The BCP coated substrate is then used as a template for patterning catalyst arrays and finally selective CVD growth of CNTs on patterned arrays (Figure 3-14).

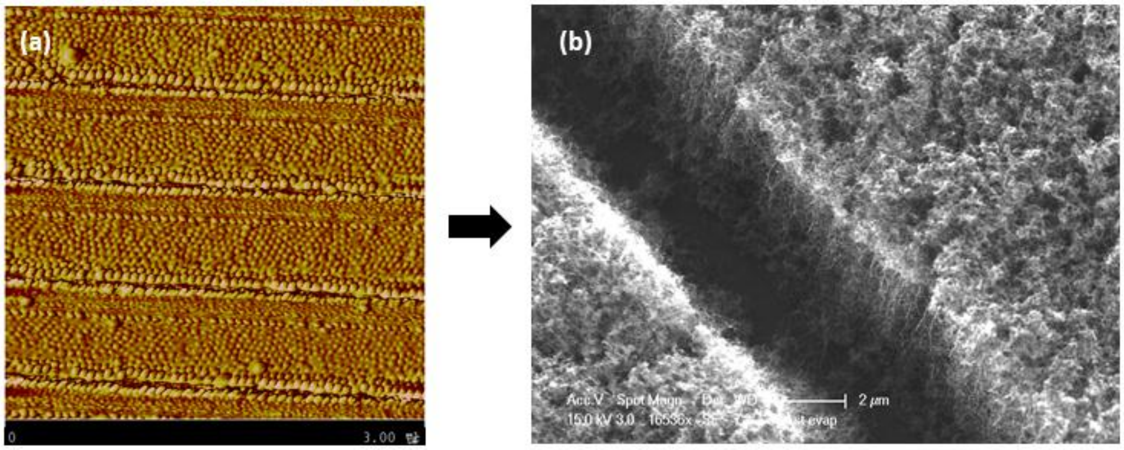

Figure 3-13 (a) AFM image of PS-b-P2VP coated on top of NIL fabricated pattern, (b) SEM image of selective CVD growth of CNTs on the BCP patterned arrays of Fe catalyst

3. 6 Conclusion

In this chapter, after explaining the basic concept of microphase separation, block copolymers as a class of self-assembly materials with attractive patterning features have been introduced. It has been demonstrated that block copolymers provide effective and promising strategies for nanofabrication of functional nanostructures. Next, the experimental strategies for developing and alignment of different diblock copolymer morphologies have been described and discussed. Since the final goal of this work is to use BCP domains for fabrication of arrays of catalytic nanodots, more emphasis has been concentrated on the alignment of cylindrical Block Copolymers. In our research we managed to vertically align the cylindrical nano-domains of Ps-b-PnVP diblock copolymers by use of solvent annealing technique. Following that, we discuss how we utilized aligned diblock copolymer films as templates for patterning arrays of metallic catalyst nanoparticles. Fabrication of BCP assisted catalyst arrays typically include: 1- loading the block copolymer core block (PnVP in our work) with catalyst ions like Au^{+3} and Fe^{+3}, and 2- chemical reduction of BCP-organized metallic ions, with Plasma treatment. We demonstrated and discussed the BCP-patterned gold and iron catalyst arrays with AFM, SEM, and TEM. BCP-patterned catalyst arrays were then utilized for chemical vapor deposition (CVD) growth of carbon nanotubes. The results of CVD synthesis confirm the superior nano-patterning capability of block copolymers and their potential to build next generation of carbon nanotube-graphene hybrid structures.

Finally, we showed selective growth of CNTs on targeted patterns by combining lithography patterning techniques with polymer self-assembly strategies. The growth results suggest that top-down pattern assisted self-assembly of BCPs can effectively control the organization of catalyst arrays, and accordingly, the carbon nanostructure that are grown on these catalyst foundations. We believe that it is unlikely that a single technique will be able to satisfy all the requirements and lead all areas of nanofabrication. Therefore, topographically assisted self-assembly method, where two fundamentally different fabrication techniques are merged into one hybrid nanomanufacturing approach, points towards the future design of high-volume functional nanostructures.

3.7 References

[1] M. Lazzari, G. Liu, and S. Lecommandoux; “Block Copolymers in Nanosciene”, WILEY-VCH Verlag GmbH&Co. KGaA, Weinheim (2006)

[2] I. W. Hamley; “Developments in Block Copolymer Science and Technology”, John Wiley & Sons (2004)

[3] N. Hadjichristidis, S. Pispas, G. Floudas, “Block Copolymers: Synthetic Strategies, Physical Properties, and Applications”, John Wiley & Sons (2002)

[4] F. B. Calleja, Z. Roslaniec, “Block Copolymers”, CRC Press (2000)

[5] M. Di Ventra, S. Evoy, J.R. Heflin Jr., “Introduction to Nanoscale Science and Technology”, Springer (2004)

[6]. M. P. Stoykovich, M. Müller, S. O. Kim, H. H. Solak, E. W. Edwards, J. J. de Pablo and P. F. Nealey, Science 308 (5727), 1442-1446 (2005).

[7] S. O. Kim, H. H. Solak, M. P. Stoykovich, N. J. Ferrier, J. J. de Pablo, P. F. Nealey, Nature, 424(6947), 411-414 (2003)

[8] R. A. Segalman, A. Hexemer and E. J. Kramer, Macromolecules 36 (18), 6831-6839 (2003).

[9] S. Park, B. Kim, J. Xu, T. Hofmann, B. M. Ocko, T. P. Russell, Macromolecules, 42(4) 1278-1284 (2009)

[10] S. Park, J.-Y. Wang, B. Kim, W. Chen, T. P. Russell, Macromolecules, 40(25) 9059-9063 (2007)

[11] B. Kim, S. Park, T. J. McCarthy, T. P. Russell, Small, 3(11) 1869-1872 (2007)

[12] S. Park, J.-Y. Wang, B. Kim, T. P. Russell, Nano Lett.2009, 8 (6), pp 1667–1672

[13] S. Park, D. H. Lee, J. Xu, B. Kim, S. W. Hong, U. Jeong, T. Xu, and T. P. Russell, Science, 323, 1030-1033(2009)

[14] T. Thurn-Albrecht, J. Schotter, G. A. Kästle, N. Emley, T. Shibauchi, L. Krusin-Elbaum, K. Guarini, C. T. Black, M. T. Tuominen and T. P. Russell, Science 290(5499), 2126-2129 (2000).

[15] T. Thurn-Albrecht, R. Steiner, J. DeRouchey, C. Stafford, E. Huang, M. Bal, M. Tuominen, C. J. Hawker and T. P. Russell, Advanced Materials 12(15), 787 (2000).

[16]. R. Glass, M. Arnold, E. A. Cavalcanti-Adam, J. Blümmel, C. Haferkemper, C. Dodd and J. P. Spatz, New Journal of Physics 6 (1), 101 (2004).

[17] G. Kästle, H.-G. Boyen, F. Weig, G. Leng, T. Herzog, P. Ziemann, S. Riethmüller, O. Mayer, C. Hartmann, J.P. Spatz, M. Möller, M. Ozawa, F. Banhart, M.G. Garnier, P. Oelhafen, Advanced Functional Materials, 13(11), 853-861(2003).

[18] J.P. Spatz, V.Z.-H. Chan, S. Mößmer, F.-M. Kamm, A. Plettl, P. Ziemann, M. Möller, Advanced Materials, 14(24), 1827-1832 (2002).

Chapter 4

4. Non-invasive High-Throughput Metrology of Doped Graphene

4.1 Introduction

So far, the electronic attributes of graphene stand out as one of its greatest selling points and have been the subject of most of graphene research efforts. Such attractive features include high charge carrier mobility,[17] unique band structure,[18] and unconventional quantum hall effect.[3, 19] Recently, graphene-based field-effect transistors (GFETs) have been introduced as a prospect for post-silicon electronics.[20, 21] For fabrication of devices and interconnects, however, the electrical properties of graphene need to be modulated.

The materials presented in this chapter are based on our previous publications: Ghazinejad et al., Advanced Functional Materials, DOI: 10.1002/adfm.201200434; and Reiber Kyle et al, Small, DOI: 10.1002/smll.201190068

Chemical doping, a major approach for tuning electronic properties, has been consistently applied in semiconductor materials to control the type and density of charge carriers.[22, 23] A variety of chemical methods have been reported for functionalizing graphene to n- and p-type, which are required for complementary metal oxide semiconductor (CMOS) materials and, accordingly, logic circuits.[24] As the graphene processing methods develop, the need for high-throughput metrology techniques, capable of mapping functionalized areas on a large scale, keeps recurring.[22, 23, 25, 26]

Characterization techniques such as electron microscopy, scanning probe microscopy, Raman spectroscopy, and X-ray photoemission spectroscopy allow measurement of specific properties against metrics of interest, including defects, uniformity, and Fermi level. While these techniques provide valuable information about electronic and structural properties of graphene at an atomic-level, they are often slow and encompass only small regions. For example, mapping a 1cm^2 graphene sheet with a coarse mesh of 1 point per 100μm requires 10,000 measurements. Because each collection point requires about 30-60 seconds, such a measurement would take around 150 hours.

Recognizing the benefit of a high-throughput optical metrology, a few studies focused on exploiting graphene's photophysical properties to visualize it.[26-29] Treossi et al. utilized fluorescence quenching to visualize graphene on a fluorescent-dye functionalized substrate.[28] Building on this concept, Kim et al. employed the fluorophores in the form of a fluorescent-polymer deposited layer to visualize exfoliated graphene and reduced graphene oxide sheets.[26] Recently, we developed a graphene-metrology technique that utilizes fluorescence quenching of DCM dye by graphene. Quantifying the extent of fluorescence quenching via image processing allowed us to achieve centimeter-scale metrology of layer thickness and uniformity of entire CVD-grown graphene sheets.[30] In contrast to the current sequential characterization techniques that record one data point at a time, FQM technique provides high-throughput identification of graphene, up to diffraction limit, at a single recording.[26, 30]

4.2 Background: Fluorescence Quenching Metrology for Identifying Graphene Atomic Planes

Fluorescence quenching are photophysical processes by which the fluorescence intensity of a fluorophore decreases through different mechanisms. In most processes, the quenching occurs through the addition of energy acceptor materials to a fluorescent system. The introduction of the quenching agent molecule (acceptors) results in non-radiant energy transfer processes between the fluorophore (donor) and the quencher (acceptor). The main mechanisms by which dynamic fluorescence quenching takes place are Förster resonant energy transfer and Dexter electron transfer. In Förster resonant energy transfer (FRET), that is considered a long-range phenomenon, quenching happens due to dipole–dipole interaction and the spectral overlap between the donor and acceptor. Dexter electron transfer, however, is based on electron exchange between donor and acceptor due to the spatial overlap of their molecular orbitals. Accordingly Dexter mechanism quenches fluorescence in much shorter distance between the fluorophore and quencher, than FRET mechanism.

Fluorescence quenching microscopy (FQM) is a visualization technique that relies on reduction of fluorescence quenching of fluorescent dyes by the material that is to be visualized. Owing to graphene attractive photophysical behavior, FQM is a highly effective approach for large-scale characterization of graphene-based materials. Here, we focus on evolving fluorescence quenching microscopy from a simple visualization tool to a basis for high-throughput metrology approach that paves the way for realistic industrial application of graphene materials and their 2D interfaces.

Standard procedure for FQM imaging includes coating the graphene sheets with a dye doped polymer solution, followed by imaging the graphene sample with a fluorescence microscope. From this point, image processing techniques will be employed to develop a montage image of an entire graphene samples for wafer-scale identification of the number of the atomic planes and defects.[37] Before developing the montage image, the collected images should be processed to remove the effects of nonuniform illumination (Figure 4-1). [37]

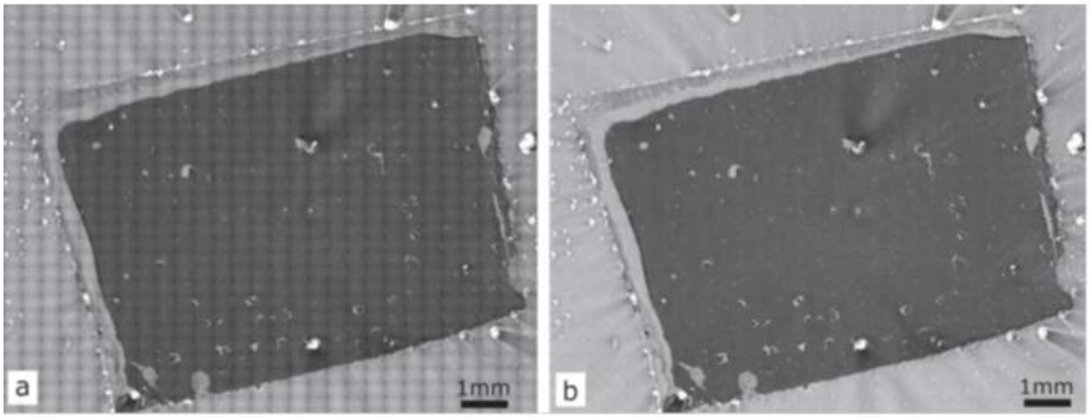

Figure 4-1 Montage fluorescence image of dyed graphene sample a) before and b) after image processing to remove the the effects of nonuniform illumination.[37]

Quantitative analysis of quenching contrast by graphene layers can determine number of graphene atomic plane on the regions of interest. To this end, first we find the unquenched fluorescence intensity of the coated dye on the background substrate. Subsequently, analysing the histogram of the montage wafer-scale image allows us to determine the intensity contrast ranges that correspond to different number of graphene layers. The graphene quenched contrast ranges are calculated relative to the fluorescence intensity of unquenched background that we determined in the first step.

$$C = \frac{I_{background} - I_{x,y@graphene}}{I_{background}} \tag{1}$$

We employ 4-(dicyanomethylene)-2-methyl-6-(4-dimethylaminostyryl)-4H-pyran (DCM) as the fluorescent agent. DCM is dispersed in polymethylmethacrylate (PMMA) then coated onto the graphene surface. For a 30-nm-thick DCM-PMMA layer, the measured contrast ranges for graphene layers relative to the unquenched substrate are calculated from the above-mentioned formula as follows [37]:

$$\text{Layer No. } (x, y) = \begin{cases} 0.75 \le C < 0.80, & 3+ \text{ layers} \\ 0.58 \le C < 0.75, & 2 \text{ layers} \\ 0.35 \le C < 0.58, & 1 \text{ layer} \end{cases} \tag{2}$$

Similar contrast quantification procedure can be employed to identify defects and/or contamination on graphene samples. [37]

Finally, we map image pixels to graphene layers and regions based on their contrast value. This mapping produces a segmented image of entire graphene sheet that can be presented by assigning exclusive colors to different layers and regions of graphene sample (Figure 4-2). [37]

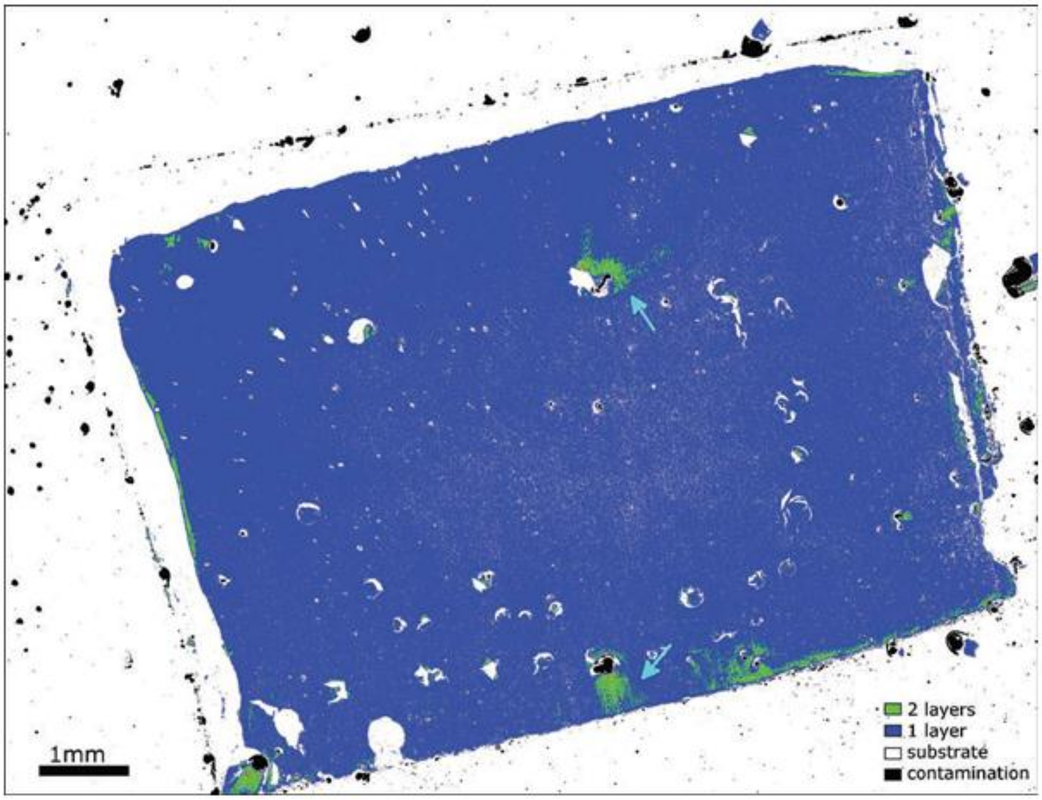

Figure 4-2 Large-scale segmented image of a dyed CVD graphene sample showing different graphene layers and surface contamination. [37]

After a brief description of FQM metrology, in the rest of this chapter we focus on the capability of our FQM metrology to visually differentiate regions of doped and pristine graphene. Through analysis of the fluorescence image histograms, we calculate distinctive intensity ranges that correspond to functionalized and as-grown graphene. Spectroscopic studies of photo-physical properties of the dye revealed that an increase in non-radiative decay rates in the presence of graphene were the principal reason for the observed emission quenching. We also improve upon the FQM image segmentation algorithm by implementing Gaussian curve fitting to dynamically determine the contrast ranges corresponding to graphene regions. This work represents a significant augmentation for FQM; since in addition to its ability to determine layers and homogeneity of large-scale graphene, it can now visualize and map doped regions in CVD-grown graphene sheets.

4.3 Graphene Growth, Doping, and Fluorescence Imaging

Graphene Growth: 25µm-thick copper foils (from Alfa Aesar, cut into 1cm^2) were chosen as the catalyst substrate. The copper foil was etched with acetic acid at 35^{o}C for 10minutes to remove any copper oxide on the foil's surface. After washing the foils completely with deionized (DI) water, we loaded them into a CVD chamber and heated them to 1000°C under 5-Torr pressure. Once the temperature was stabilized at 1000°C, the catalyst substrates (foils) were annealed for 30 minutes under a 100/100 sccm flow of hydrogen and argon gas. Next, the argon feed was stopped and a methane gas flow of 100 sccm was introduced into the tube for 20 minutes to begin the chemical vapor deposition of graphene on copper. All flow rates were precisely controlled using mass flow controllers. Upon completion of the CVD growth, methane gas feed were stopped and the furnace was cooled to room temperature under the protection of argon gas flow. Graphene sheets, grown on copper foils, were removed from the CVD chamber, covered with PMMA by spin coating, and heated at 100°C for 10 minutes to bake the PMMA layer. Next, the graphene sheets were removed from the copper film by etching in a 0.3M aqueous $FeCl_3$ solution, followed by rinsing with an aqueous HCl (4%) and DI water solution. Graphene samples were then allowed to relax on the glass substrates overnight before they were dipped in acetone to remove the PMMA layer. [37]

Graphene Fluorination: For patterned fluorination, a CVD graphene sheet immobilized on a glass substrate was spin-coated with a photoresist layer. Next, photolithography was performed using a patterned mask having circular and stripe windows to define the areas to be fluorine-treated. Upon development of the mask, graphene sheets were selectively fluorinated using a reactive ion etching (RIE) machine. The plasma treatment was carried out at room temperature with the CF_4 gas pressure fixed at 10 mTorr, while the CF_4 flow rate was kept constant at 50 sccm. Graphene fluorination was performed with 10 seconds of plasma exposure at an RF power level of 25W. [41] After dissolving the photoresist in acetone overnight, selectively fluorinated graphene was dried and prepared for dye coating.

Dye Preparation and Coating: The fluorescent dye mixture consisted of 1 wt% PMMA (M_w = 120,000) and 0.01 wt% 4-(dicyanomethylene)-2-methyl-6-(4-

dimethylaminostyryl)-4H–pyran (DCM Sigma-Aldrich) in toluene (>99.5% Fisher Chemical). The dye solution was stirred and heated overnight to dissolve the polymer, then continuously kept stirring while stored. Immediately before the solution was spun onto the substrate it was sonicated for 15 minutes, and passed through a 0.22μm filter to ensure homogeneity of the dye solution and to avoid unnecessary contamination. The polymer-dye was then spin-coated onto the surface of the graphene at 3000 rpm for 60 seconds. The thickness of coated dye-polymer layer is 30 nm, measured with Dektak 8 Surface Profilometer. Once coated, the graphene was placed in a desiccator for at least 1hour to ensure the complete evaporation of the solvent and maintain a consistent layer thickness of the dye on different graphene samples.

Fluorescence Microscopy: A BD Pathway 855 HT confocal microscope with an arc lamp light source was used to acquire the images. The light path of the incident light consisted of a 470nm bandpass filter and a 520nm dichroic filter. The light then passed through an Olympus 20x objective lens with 0.75 NA and was emitted through a 542nm bandpass filter before being detected by a CCD camera. The final images were produced using a montage of smaller images that captured 417x318μm^2 sections of the sample in order to maintain high resolution over a large area. The images were obtained with the help of BD AttoVision software.

Emission and absorption spectroscopy: Diffuse reflectance spectroscopy allowed us to obtain UV/visible absorption spectra of the solid-film samples using a JASCO V-670 spectrophotometer (Tokyo, Japan), equipped with a 60 mm ψintegrating sphere equipped with an individual detector (Model ISN-723, JASCO, Japan). Aluminum foil was used as a reflector for the blank slides and for all the samples. We determined the absorbance, $A = -2\log(R)$, from the reflectance, R, where the factor 2 was added to account for the reflector on the back of the transparent substrates.

Steady-state emission spectra and time-resolved emission decays were recorded using a FluoroLog-3 spectrofluorometer (Horiba-Jobin-Yvon) equipped with double-grating monochromators and a TBX single-photon-counting detector. Small-angle fluorescence spectroscopy settings allowed for collecting the emission signal at 22-degree angle from the incident excitation light. [55] From the steady-state absorption and emission data we calculated the fluorescence quantum yields. [56] Rhodamine 3B (R3B) was used as a standard: Φ_f of R3B in ethanol is 0.45. [57]

For recording the emission decays, we used the time-correlated single-photon counting (TCSPC) setup of the spectrofluorometer, employing pulsed diode laser for excitation source (406 nm, half-height pulse width = 195 ps). Bi-exponential data fits, involving deconvolution of the emission decay data, yielded the lifetimes, τ_i, and the corresponding weighing pre-exponential coefficients, f_i (Table 1). [58]

Image Processing: All image processing was performed using custom scripts in Matlab v7.4. For flat-field correction, the following flat-field correction algorithm was applied to each individual image in the large-area fluorescence montage:

$$I_{flat} = \frac{I_{original}}{I_{correction}} \times \overline{I_{correction}} \tag{3}$$

The correction image used in this algorithm has the same dimensions as the original individual images to be corrected and was taken of the bare substrate using the same optical settings used to collect the large-area montage. *[37]*

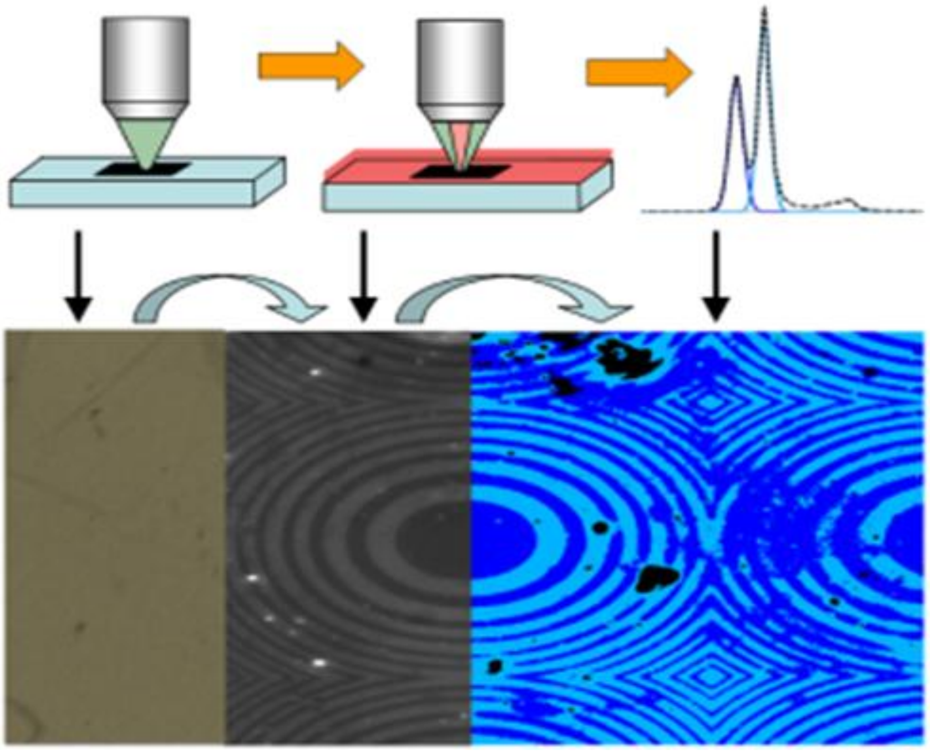

Figure 4-3 Procedure of fluorescence quenching microscopy (FQM) for quick visualization of doping in relatively large regions of graphene. [59]

4.4 FQM Metrology of Pristine and Doped Graphene Sheets

Chemical functionalization of graphene often results in disruption of sp2-hybridization of carbon atoms, change in Fermi level, and accordingly, change in the excitation energy of graphene.[25, 38, 39] Therefore, we expect FQM to allow identification of chemically treated graphene through reduced quenching.

We performed chemical functionalization through fluorination of graphene via reactive ion plasma etching since it allows generation of complex functionalization patterns through lithography techniques. Fluorination of graphene offers a practical route for the optical and electronic modifications needed for a number of graphene device applications.[38, 40] Following the procedure outlined in [41], we fluorinated selected areas of CVD-grown graphene sheets with CF_4 plasma and striped protective masks. The graphene samples were then coated by a DCM –PMMA solution, as described in our previous work.[37]

To visualize functionalized regions of CVD graphene, we collected FQM images of fluorinated CVD graphene (Figure 4-4). Fluorinated and pristine regions of the CVD graphene sample were detectable in the original collected large-area fluorescence montage; however, individual images had dark outlines due to uneven illumination (Figure 4-4a). It should be noted that large-area fluorescence montage image allows for unbounded large-scale mapping of the graphene sample without compromising the necessary resolution. Using a low-magnification objective would deteriorate mapping resolution. Furthermore, there is a limit to the area that even a very low-magnification objective can image. Flat-field correction was used to remove the effect of uneven illumination in the individual images, resulting in a uniform large-area image (Figure 4-4b). In FQM, regions are identified by their intensity contrast relative to the unquenched fluorescence peak in the image histogram.[37] Contrast between two regions in fluorescence quenching is given by:

$$C_{2-1} = \frac{I_1 - I_2}{I_1} \qquad (4)$$

When region 1 is the bare glass substrate, which does not quench the dye layer fluorescence emission, contrast is equal to the fluorescence quenching factor of graphene in region 2. The original FQM image segmentation algorithm applied fixed contrast ranges to all FQM images for identifying graphene layers. These contrast ranges were experimentally determined. In this work, we improve upon the FQM image segmentation algorithm by implementing Gaussian curve fitting to automatically and dynamically determine the contrast ranges corresponding to graphene regions.

To perform Gaussian curve fitting, the user enters the rough location of the image histogram peaks and the height, width, and location parameters of the histogram-fitted Gaussian curves are automatically determined. Our algorithm utilizes the 'fminsearch' function provided by Matlab to fit the Gaussian curves to the histogram peaks. The 'fminsearch' function implements the Nelder-Mead simplex method.[42, 43] The Nelder-Mead algorithm is an iterative function-minimization method, in our case employed to minimize the error function measured between the Gaussian curve to be fitted and the image histogram.

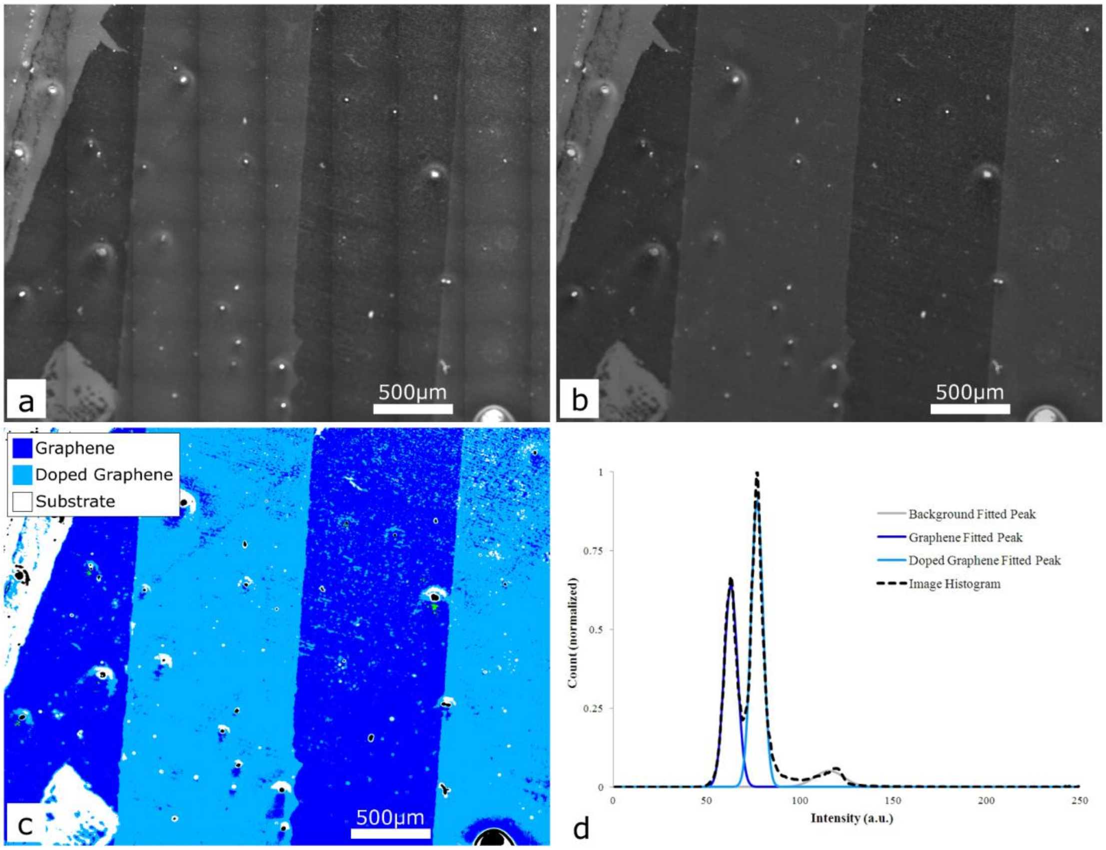

Figure 4-4 Fluorescence images of CVD graphene fluorine-doped using a striped mask (a) before and (b) after flat-field correction. Fluorescence quenching metrology segmented image (c) showing the pristine graphene regions (dark blue) and doped graphene regions (light blue). The fluorescence image histogram and fitted Gaussian peaks corresponding to the substrate (grey), doped graphene (light blue), and pristine graphene (dark blue) (d). [59]

Our segmentation algorithm segments the FQM image by mapping pixels within the image to regions according to their intensity contrast relative to the background signal, taken as the location of the Gaussian curve fitted to the substrate fluorescence intensity peak in the image histogram. Contrast ranges corresponding to segmented regions are bounded at the intensity values where the fitted Gaussian curves overlap. This algorithm successfully segments the corrected FQM image into pristine graphene, doped graphene, glass substrate, and contamination (black) regions (Figure 4-4c). The contrast (C) ranges, determined from Gaussian curve fitting of the fluorescence image histogram (Figure 4-4d), are:

$-0.2 \leq C < 0.217$ – substrate,

$0.217 \leq C < 0.391$ – doped single-layer graphene,

$0.391 \leq C < 0.58$ – pristine single-layer graphene,

$C < -0.2$, $C > 0.58$ – contamination

Contrast between pristine graphene and the substrate, measured between the peaks of the fitted Gaussian curves, is 48%. This value is in agreement with the results from the original FQM segmentation algorithm, published previously.*[30]* Contrast between doped graphene and the substrate is reduced to 32% and contrast between doped graphene and pristine graphene is 23%.

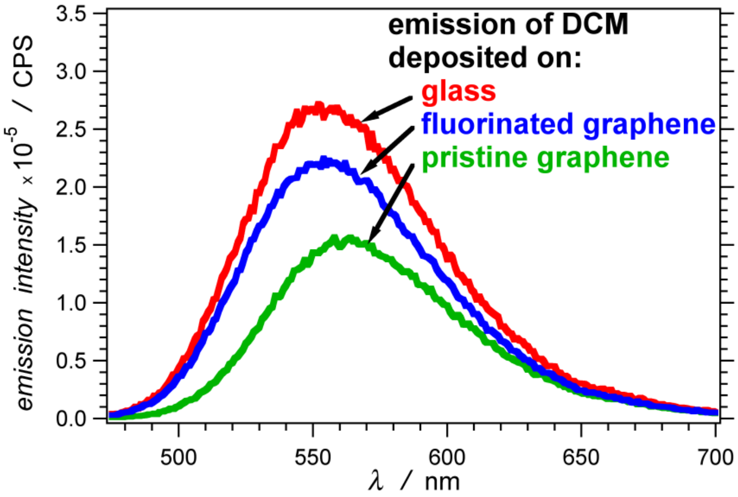

Figure 4-5 Fluorescence spectra of the 30-nm DCM-PMMA (1% w/w) layer over bare glass, fluorinated graphene, and pristine graphene (λ_{ex}= 460 nm).[59]

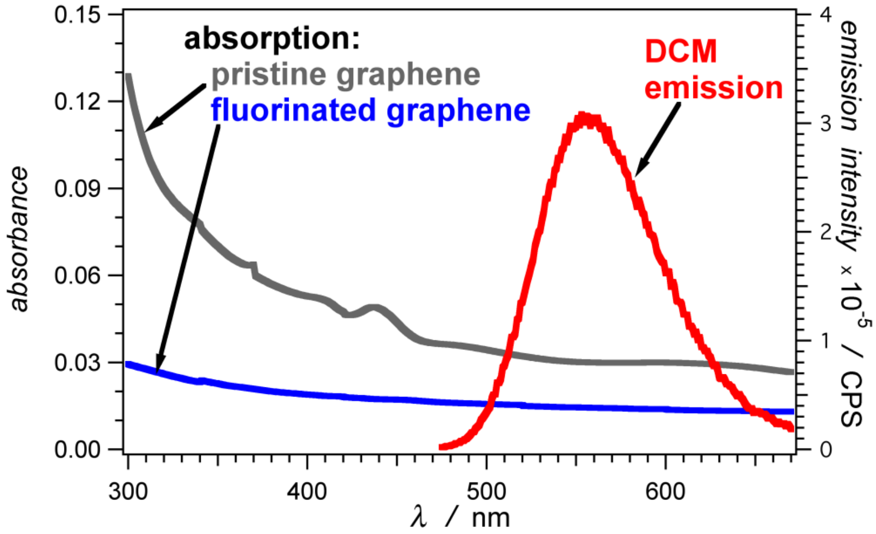

Figure 4-6 Overlap of the emission spectrum of DCM-PMMA film with the absorption spectra of pristine and fluorinated graphene. [59]

In FQM, not all of the fluorophores in the dye layer are quenched by graphene. Therefore, the measured fluorescence emission is a combination of signals from quenched and unquenched fluorophores. As quenching increases, the ratio of quenched fluorophores to unquenched fluorophores increases. The emission peak height attenuation indicates this ratio. Comparing peak heights in fluorescence emission spectra of the dye layer over the bare substrate, fluorinated graphene, and pristine graphene, we find that peak height attenuation by fluorinated graphene is approximately 25% of attenuation by pristine graphene (Figure 4-5). Therefore, while both fluorinated and pristine graphene quench fluorescence emission, quenching potency of fluorinated graphene has been noticeably reduced. Upon fluorination the absorptivity of graphene, and thus the spectral overlap with emission of DCM, decreased (Figure 4-6). When quenching occurs due to charge transfer mechanism, its efficiency and FQM image would strongly depend on change in Fermi level and type of chemical doping. Conversely, when the quenching occurs due to energy transfer mechanism its efficiency is primarily affected by absorptivity. *[44]*

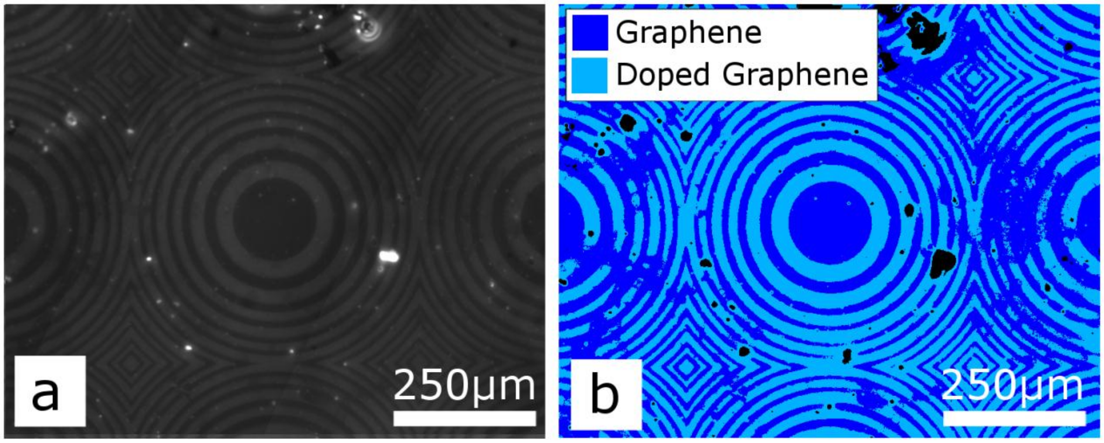

Figure 4-7 Original fluorescence (a) and fluorescence quenching metrology-segmented (b) images of CVD graphene fluorinated using a circle mask. [59]

To demonstrate the efficacy of FQM for visualizing complex chemical functionalization patterns, we used a high-resolution circular photolithography mask to fluorinate a CVD graphene sample and collected FQM images of the fluorinated sample. The fluorinatation pattern is readily visible in the original fluorescence image (Figure 4-7a) and segmentation (preceded by flat-field correction) accurately maps functionalized and pristine regions (Figure 4-7b). In this sample, contrast between fluorinated graphene and pristine graphene (determined from fitted Gaussian curve locations) is only 17%, which is smaller than the 23% contrast observed in the sample fluorinated using the simple striped mask (Figure. 4-4). This reduced contrast between the fluorinated and pristine regions indicates reduced chemical treatment efficacy with the complex circular pattern. Unlike graphene layers, which always have the same quenching contrast, fluorinated regions have variable quenching contrast due to variations in the fluorination intensity. Therefore, a segmentation algorithm cannot identify chemically modified regions using fixed contrast ranges. However, because our segmentation algorithm uses Gaussian curve fitting to automatically determine dynamic contrast ranges, the fluorinated regions are accurately identified and mapped in the segmented image (Figure 4-7b).

4.5 Characterization of Photo-Physical Properties of Pristine and Doped Graphene

To investigate the change in graphene structure due to chemical functionalization we employed Raman spectroscopy technique.[45] Raman spectroscopy allows for resolving bonding patterns in graphene sheets and offers insight on the changes in electronic state and structure of graphene due to chemical and electrical doping.[46-48]

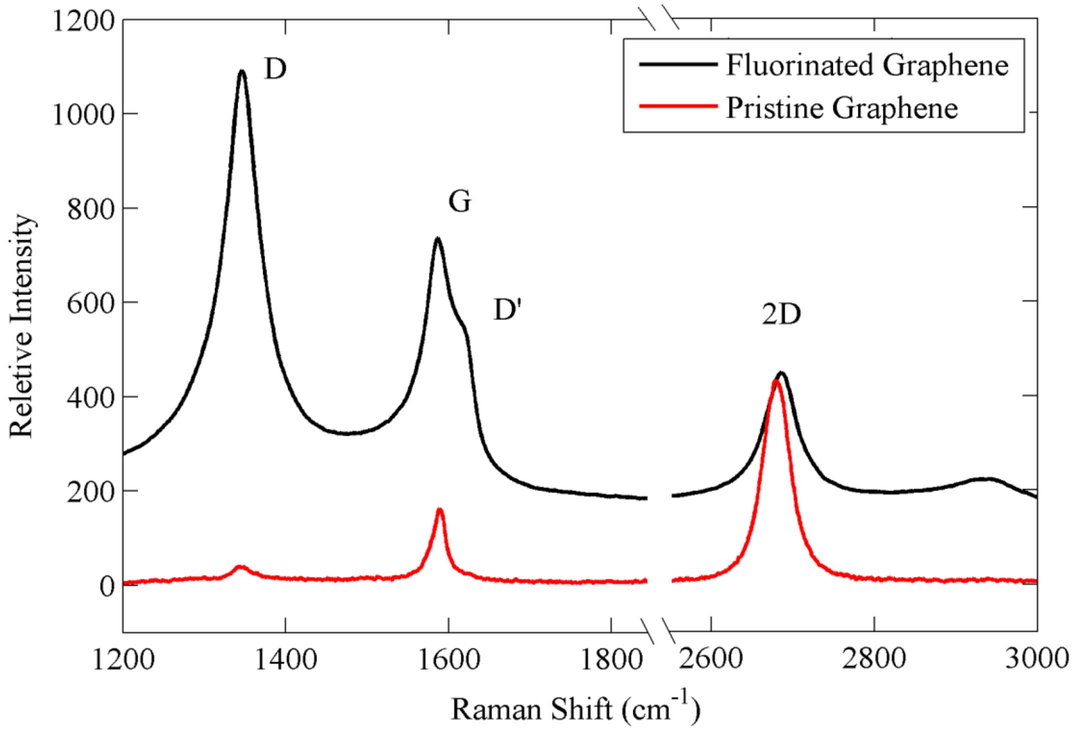

Figure 4-8 Raman spectra of pristine (bottom) and fluorinated (top) graphene (λex = 532 nm).[59]

A typical Raman spectrum collected from our CVD-grown graphene sheet is shown in Figure 4-8. The G band, centered on 1580cm^{-1}, is the first-order Raman mode induced by in-plane vibration of carbon atoms in sp^2-hybridized graphene sheets. As a result, the intensity and sharpness of G band signify the presence of crystalline graphitic phase in the synthesized material. The D band at 1335cm^{-1} is the defect-originated second-order Raman band which indicates the level of disorder in graphitic sp^2 structures. The nature of this band is related to one-phonon elastic scattering and it is interpreted as a measure of the quantity of sp^3 or dangling sp^2 bonds that are causing structural disorders. The 2D-band at 2600cm^{-1}, on the other hand, is originated by an inelastic scattering processes that involve phonons. This band is sensitive to the number of layers and is more pronounced in single- to few-layer graphene. Thus, a 2D/G intensity ratio has been consistently used to determine the thickness of graphene sheets. The collected Raman spectra verify that the CVD-grown graphene sheet has a very low defect level and is primarily single- to bi-layer.

Several studies on carbon nanotubes and carbon bulk materials showed that formation of sp^3 bonds, which are produced from breaking of the sp^2 network in graphene, contributes to an increase in the D peak intensity.[38, 47, 48] As a result, any type of chemical doping, or process in general, that yields such a distortion in hybridization of carbon atoms would affect the ratio of D band to G band peak intensities, I_D/I_G. We observed that the intensity of the D peak of fluorinated graphene was much larger than that of the G and 2D peaks, and therefore I_D/I_G ratio increased considerably. Because the D peak represents transitions between vibrational states associated with the sp^3 defects, its presence indicates an increase in the degree of disorder. The ratio of 2D band and G band peak, I_{2D}/I_G, is also susceptible to chemical doping, as it generally reduces 2D band intensity.[36, 47, 48] Thus, while chemical doping usually escalates I_D/I_G, it reduces I_{2D}/I_G.[36, 49] Such behavior was echoed by the Raman spectra that we collected from the fluorinated graphene sample (Figure 4-8).

To characterize the quenching of the DCM fluorescence by graphene, we employed UV/visible spectroscopy. Comparison between the steady-state emission spectra of PMMA-DCM films coated on bare glass and on glass-immobilized graphene showed a decrease in the fluorescence intensity of the dye in the presence of the carbon allotrope (Figure 4-5).

Table 4-1 Photophysical properties of DCM coatings of glass and graphene samples.[a]

sample	Φ_f	τ_1 / ns (f_1) [b]	τ_2 / ns (f_2) [b]	$\langle\tau\rangle$/ ns [c]	$k_r\times10^{-8}$/ s^{-1} [d]	$k_{nr}\times10^{-8}$/ s^{-1} [e]	$k_Q\times10^{-8}$/ s^{-1} [f]
Bare Glass	**0.72**	**1.82 (0.69)**	**3.65 (0.31)**	**2.69**	**2.7**	**1.0**	**0**
Doped Graphene	**0.57**	**1.33 (0.66)**	**3.40 (0.34)**	**2.49**	**2.1**	**1.9**	**0.9**
Pristine Graphene	**0.39**	**1.13 (0.74)**	**2.90 (0.26)**	**1.96**	**2.0**	**3.1**	**2.1**

[a] DCM was dispersed in PMMA, and the dye-doped polymer was deposited as 30-nm thick films on bare glass, and on glass-immobilized single-sheet graphene samples.

[b] From exponential fits of TCSPC-measured emission decays: ⍰$_{ex}$ = 406 nm (pulse half-height width = 195 ps); ⍰$_{ex}$ = 566 nm.

[c] Average lifetime: $\langle\tau\rangle = (f_1\tau_1^2 + f_2\tau_2^2) / (f_1\tau_1 + f_2\tau_2)$.

[d] Apparent radiative-decay rate constant: k_r = ⍰$_f /\langle\tau\rangle$.

[e] Apparent non-radiative-decay rate constant: k_{nr} = (1 − ⍰$_f$) $/\langle\tau\rangle$.

[f] Apparent emission-quenching rate constant: $k_Q = k_{nr} - k_{nr}^{(\text{bare glass})}$.

Correcting for the amount of light absorbed, as estimated from the absorbance of the dye in the polymer films, revealed that pristine graphene caused almost two fold decrease in the emission quantum yield of DCM, Φ_f, in comparison with the samples on bare glass (Table 4-1). Concurrently, the emission quantum yield of DCM dispersed in a polymer film coated over fluorinated graphene was larger than Φ_f in presence of pristine graphene but still smaller than Φ_f for the films on bare glass (Table 4-1). Thus, the fluorinated graphene did not quench the DCM emission as efficiently as the pristine graphene, which was consistent with our observations with the fluorescence microscopy (Figures 4-4 and 4-7).

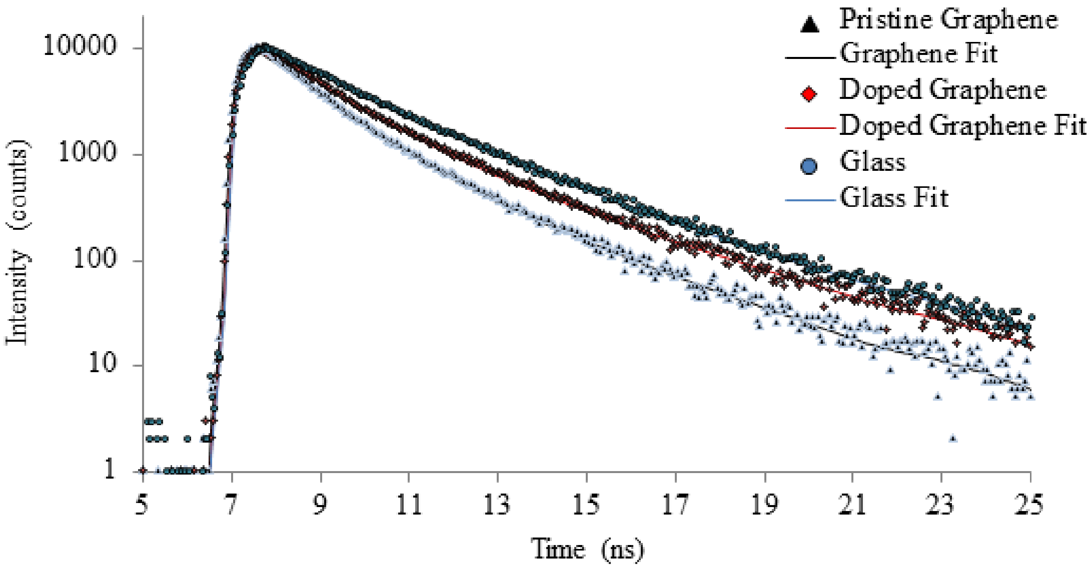

Figure 4-9 Fluorescence decays of 30-nm DCM-PMMA layer (1% w/w) over bare glass, fluorinated graphene, and pristine graphene. λ_{ex} = 406 nm (pulse half-height width = 195 ps); λ_{em} = 566 nm. [59]

To quantify the DCM excited-state kinetics and elucidate the processes responsible for the observed fluorescence quenching, we resorted to time-resolved emission spectroscopy. The lack of linearity in the decays of the intensity of the DCM emission, when plotted against logarithmic ordinate (Figure 4-9), indicated that the deactivation of the emissive excited state of the dye did not have a mono-exponential character. This observation was consistent with the heterogeneity of the solid samples, requiring multi-exponential analysis. As previously reported in *[50]*, bi-exponential functions provided the simplest mathematical expression that could successfully fit the emission decays of DCM (Table 4-1). The average lifetimes, $\langle \tau \rangle$, obtained from the bi-exponential fits, manifested a similar trend as the emission quantum yields (Table 1). While $\langle \tau \rangle$ of DCM deposited over bare glass was 2.69 ns, $\langle \tau \rangle$ of DCM in the presence of pristine graphene was 1.96 ns (Table 4-1).

From Φ_f and $\langle \tau \rangle$ we estimated the rate constants of the radiative, k_f, and non-radiative, k_{nr}, processes responsible for the deactivation of the DCM excited state (Table 1). Graphene had a relatively small effect on k_f. For samples with and without graphene, the values of k_f varied within about 30%, from 2.0×10^8 s^{-1} to 2.7×10^8 s^{-1} (Table 1), which was expected since graphene should not affect the electronic structure of the DCM molecules in order to alter its radiative decay rates. The carbon allotropes, however, considerably affected the non-radiative decay rates. The presence of pristine graphene caused a three-fold increase in k_{nr} in comparison with the sample of dye-polymer films deposited on bare glass (Table 4-1). These findings allowed us to estimate the apparent *pseudo*-monomolecular quenching rate constants, k_Q: 2.0×10^8 s^{-1} and 8.4×10^8 s^{-1} for pristine and fluorinated graphene, respectively (Table 4-1).

Our photophysical findings, considered along with the structural properties of the samples, suggested that the observed emission quenching resulted predominantly from resonance energy transfer.[51-53] Processes requiring at least adequate electronic coupling between the dye and the graphene, such as charge transfer and electron-exchange energy transfer, are inefficient at donor-acceptor distances exceeding about two nanometers.[54] Considering the 30-nm-thick coated polymer-dye layer, measured by a surface profilometer, such electron-transfer processes would be unfeasible for more than 90% of the DCM molecules in the polymer film, and hence could not explain the observed 46% decrease in Φ_f in the presence of graphene (Table 4-1). Conversely, the donor-acceptor distances at which Förster resonance energy transfer (FRET) is efficient are comparable with the thickness of the dye-doped polymer films that we used. Furthermore, fluorination of the pristine graphene decreases its absorptivity in the spectral region where DCM emits. Concurrently, k_Q for fluorinated graphene was more than twice smaller than k_Q for pristine graphene (Table 4-1), which was consistent with a decrease in the FRET rate as a result lowering the molar extinction coefficient upon fluorination of the graphene, which was the energy acceptor.

4.6 Conclusions

After the development of fluorescence quenching microscopy for metrology of centimeter-scale CVD-grown graphene sheets, we are still exploring different capabilities of the method. Given that our approach is based on quenching phenomena, investigating the parameters involved in graphene quenching enables us to methodically realize versatile potentials of this new promising metrology technique. Herein, we demonstrate the aptitude of FQM for accurately visualizing doped regions in graphene sheets. Our inspiration for this work was the modifications that doping processes cause on the chemical and electronic state of their subject materials. This, in turn, alters the fluorescence quenching condition of doped graphene, compared to that of pristine graphene. Such variation would visually differentiate doped and pristine areas of graphene when viewed under a fluorescence microscope.

In this work, first we successfully show the functionality of large-scale FQM in mapping of fluorine-doped regions in graphene sheets. To determine the method's resolution and scalability strength, we increased the complexity of the doping pattern and successfully reproduced the mapping results. Upon that, we conducted a comparative investigation on steady-state and time-resolved fluorescence parameters of dye-coated pristine graphene and fluorinated graphene, using bare glass as the control sample. The fluorometry results support the increasing trend observed in the quenching level of DCM dye, from control sample to doped graphene to pristine graphene. The variation in fluorescence quenching by graphene after it is doped is also predicted by theory, as discussed in this report. Finally, we improved our image processing technique by employing Gaussian fitting to determine the contrast regions corresponding to graphene regions. This is a valuable improvement since it facilitates the automation of the technique for production-line metrology of graphene.

The presented results imply that FQM metrologies is indeed beyond a simple fluorescence imaging technique and can visually distinguish between pristine and chemically processed regions in a very same CVD-grown sheet. This work also suggests that, with premeditated choice of dye, the interaction between fluorophores and graphene provides advantages for probing the chemical structure of functionalized graphene over large areas. Due to its simplicity, high speed, and small footprint, segmented FQM can be employed to address the chronic need for a microscopy based graphene metrology capable of "seeing" the features that are processed.

4.7 References

[1] http://nobelprize.org., **2010**, The Nobel Prize in Physics 2010

[2] K. S. Novoselov, A. K. Geim, S. V. Morozov, D. Jiang, M. I. Katsnelson, I. V. Grigorieva, S. V. Dubonos, A. A. Firsov, *Nature* **2005**, *438*, 197.

[3] K. S. Novoselov, A. K. Geim, S. V. Morozov, D. Jiang, Y. Zhang, S. V. Dubonos, I. V. Grigorieva, A. A. Firsov, *Science* **2004**, *306*, 666.

[4] Y. Zhang, Y.-W. Tan, H. L. Stormer, P. Kim, *Nature* **2005**, *438*, 201.

[5] A. K. Geim, K. S. Novoselov, *Nat. Mater.* **2007**, *6*, 183.

[6] J.-H. Chen, C. Jang, S. Xiao, M. Ishigami, M. S. Fuhrer, *Nat Nano* **2008**, *3*, 206.

[7] A. A. Balandin, S. Ghosh, W. Bao, I. Calizo, D. Teweldebrhan, F. Miao, C. N. Lau, *Nano Lett.* **2008**, *8*, 902.

[8] C. Lee, X. Wei, J. W. Kysar, J. Hone, *Science* **2008**, *321*, 385.

[9] F. Schedin, A. K. Geim, S. V. Morozov, E. W. Hill, P. Blake, M. I. Katsnelson, K. S. Novoselov, *Nat. Mater.* **2007**, *6*, 652.

[10] X. Wang, L. Zhi, K. Mullen, *Nano Lett.* **2007**, *8*, 323.

[11] J. Yan, T. Wei, B. Shao, Z. Fan, W. Qian, M. Zhang, F. Wei, *Carbon* **2009**, *48*, 487.

[12] E. Yoo, J. Kim, E. Hosono, H.-s. Zhou, T. Kudo, I. Honma, *Nano Lett.* **2008**, *8*, 2277.

[13] A. Reina, X. Jia, J. Ho, D. Nezich, H. Son, V. Bulovic, M. S. Dresselhaus, J. Kong, *Nano Lett.* **2008**, *9*, 30.

[14] X. Li, W. Cai, J. An, S. Kim, J. Nah, D. Yang, R. Piner, A. Velamakanni, I. Jung, E. Tutuc, S. K. Banerjee, L. Colombo, R. S. Ruoff, *Science* **2009**, *324*, 1312.

[15] M. P. Levendorf, C. S. Ruiz-Vargas, S. Garg, J. Park, *Nano Lett.* **2009**, *9*, 4479.

[16] S. Bae, H. Kim, Y. Lee, X. Xu, J.-S. Park, Y. Zheng, J. Balakrishnan, T. Lei, H. Ri Kim, Y. I. Song, Y.-J. Kim, K. S. Kim, B. Ozyilmaz, J.-H. Ahn, B. H. Hong, S. Iijima, *Nat Nano* **2010**, *5*, 574.

[17] V. Singh, D. Joung, L. Zhai, S. Das, S. I. Khondaker, S. Seal, *Progress in Materials Science* **2011**, *56*, 1178.

[18] X. Du, I. Skachko, A. Barker, E. Y. Andrei, *Nat Nano* **2008**, *3*, 491.

[19] A. H. Castro Neto, F. Guinea, N. M. R. Peres, K. S. Novoselov, A. K. Geim, *Reviews of Modern Physics* **2009**, *81*, 109.

[20] K. S. Novoselov, E. McCann, S. V. Morozov, V. I. Fal/'ko, M. I. Katsnelson, U. Zeitler, D. Jiang, F. Schedin, A. K. Geim, *Nat. Phys.* **2006**, *2*, 177.

[21] Y. M. Lin, C. Dimitrakopoulos, K. A. Jenkins, D. B. Farmer, H. Y. Chiu, A. Grill, P. Avouris, *Science* **2010**, *327*, 662.

[22] F. Schwierz, *Nat Nano* **2010**, *5*, 487.

[23] A. C. Diebold, *Handbook of Silicon Semiconductor Metrology*, CRC Press, **2001**.

[24] D. K. Schroder, John Wiley and Sons, **2006**.

[25] H. Liu, Y. Liu, D. Zhu, *J. Mater. Chem.* **2010**, *21*, 3335.

[26] ITRS, in *The International Technology Roadmap for Semiconductors*, **2010**.

[27] J. Kim, L. J. Cote, F. Kim, J. Huang, *J. Am. Chem. Soc.* **2009**, *132*, 260.

[28] K. M. Cromheeke, M. M. Kockx, G. R. Y. De Meyer, J. M. Bosmans, H. Bult, W. J. F. Beelaerts, C. J. Vrints, A. G. Herman, *Cardiovasc. Res.* **1999**, *43*, 744.

[29] M. E. Kose, R. J. Crutchley, M. C. DeRosa, N. Ananthakrishnan, J. R. Reynolds, K. S. Schanze, *Langmuir* **2005**, *21*, 8255.

[30] J. Kim, F. Kim, J. Huang, *Materials Today* **2010**, *13*, 28.

[31] Z. Sun, C. L. Pint, D. C. Marcano, C. Zhang, J. Yao, G. Ruan, Z. Yan, Y. Zhu, R. H. Hauge, J. M. Tour, *Nat Commun* **2012**, *2*, 559.

[32] A. Reina, S. Thiele, X. Jia, S. Bhaviripudi, M. Dresselhaus, J. Schaefer, J. Kong, *Nano Research* **2009**, *2*, 509.

[33] E. Treossi, M. Melucci, A. Liscio, M. Gazzano, P. SamoriÌ€, V. Palermo, *J. Am. Chem. Soc.* **2009**, *131*, 15576.

[34] C. M. Nolen, G. Denina, D. Teweldebrhan, B. Bhanu, A. A. Balandin, *ACS Nano* **2011**, *5*, 914.

[35] J. Wan, A. Ferreira, W. Xia, C. H. Chow, K. Takechi, P. V. Kamat, G. Jones Ii, V. I. Vullev, *Journal of Photochemistry and Photobiology A: Chemistry* **2008**, *197*, 364.

[36] C. N. R. Rao, A. K. Sood, K. S. Subrahmanyam, A. Govindaraj, *Angewandte Chemie International Edition* **2009**, *48*, 7752.

[37] J. R. Kyle, A. Guvenc, W. Wang, M. Ghazinejad, J. Lin, S. Guo, C. S. Ozkan, M. Ozkan, *Small* **2011**, *7*, 2599.

[38] J. T. Robinson, J. S. Burgess, C. E. Junkermeier, S. C. Badescu, T. L. Reinecke, F. K. Perkins, M. K. Zalalutdniov, J. W. Baldwin, J. C. Culbertson, P. E. Sheehan, E. S. Snow, *Nano Lett.* **2010**, *10*, 3001.

[39] R. Saito, M. Yagi, T. Kimura, G. Dresselhaus, M. S. Dresselhaus, *J. Phys. Chem. Solids* **1999**, *60*, 715.

[40] W.-K. Lee, J. T. Robinson, D. Gunlycke, R. R. Stine, C. R. Tamanaha, W. P. King, P. E. Sheehan, *Nano lett.*, ACS ASAP.

[41] S. Guo, M. Ghazinejad, X. Qin, H. Sun, W. Wang, F. Zaera, M. Ozkan, S. C. Ozkan, *Small* **2011**.

[42] R. A. M. J.A.Nelder *Comput. J.* **1965**, *7*, 308.

[43] J. C. Lagarias, A. R. James, H. W. Margaret, E. W. Paul, *SIAM Journal on Optimization* **1998**, *9*, 112.

[44] K. A. Velizhanin, A. Efimov, *Physical Review B* **2011**, *84*, 085401.

[45] A. C. Ferrari, J. C. Meyer, V. Scardaci, C. Casiraghi, M. Lazzeri, F. Mauri, S. Piscanec, D. Jiang, K. S. Novoselov, S. Roth, A. K. Geim, *Phys. Rev. Lett.* **2006**, *97*, 187401.

[46] D. M. Basko, S. Piscanec, A. C. Ferrari, *Physical Review B* **2009**, *80*, 165413.

[47] A. C. Ferrari, *Solid State Commun.* **2007**, *143*, 47.

[48] L. Zhao, R. He, K. T. Rim, T. Schiros, K. S. Kim, H. Zhou, C. GutiÃ©rrez, S. P. Chockalingam, C. J. Arguello, L. PÃ¡lovÃ¡, D. Nordlund, M. S. Hybertsen, D. R. Reichman, T. F. Heinz, P. Kim, A. Pinczuk, G. W. Flynn, A. N. Pasupathy, *Science*, *333*, 999.

[49] X. Dong, D. Fu, W. Fang, Y. Shi, P. Chen, L.-J. Li, *Small* **2009**, *5*, 1422.

[50] S. L. Bondarev, V. N. Knyukshto, V. I. Stepuro, A. P. Stupak, A. A. Turban, *Journal of Applied Spectroscopy* **2004**, *71*, 194.

[51] G. Gomez-Santos, T. Stauber, *Physical Review B* **2011**, *84*, 165438.

[52] R. S. Swathi, K. L. Sebastian, *J. Chem. Phys.* **2008**, *129*, 054703.

[53] R. S. Swathi, K. L. Sebastian, *The Journal of Chemical Physics* **2009**, *130*, 086101.

[54] J. R. Lakowicz, in *Principles of Fluorescence Spectroscopy,* , Springer US, Boston, MA **2006**, Ch. 9.

[55] J. Wan, M. Thomas, S. Guthrie, V. Vullev, *Annals of Biomedical Engineering* **2009**, *37*, 1190.

[56] J. Hu, B. Xia, D. Bao, A. Ferreira, J. Wan, G. Jones, V. I. Vullev, *The Journal of Physical Chemistry A* **2009**, *113*, 3096.

[57] R. F. Kubin, A. N. Fletcher, *J. Lumin.* **1983**, *27*, 455.

[58] H. Lu, D. Bao, M. Penchev, M. Ghazinejad, V. I. Vullev, C. S. Ozkan, M. Ozkan, *Advanced Science Letters* **2010**, *3*, 101.

[59] M. Ghazinejad, J. R. Kyle, S. Gue, W. Wang, V. Vullev. M. Ozkan. and C. S. Ozkan, Advanced Functional Materials, 2012, DOI: 10.1002/adfm.201200434

Chapter 5

5. Conclusions

In this work we discussed novel techniques for high-throughput fabrication and metrology of graphene materials. Our main objective here is to devise state-of–art approaches for transition of Graphene-CNT materials from laboratory to industry level applications.

In the first part of this dissertation, we reported successful synthesis of large and uniform pillared graphene films with simultaneous CVD growth of graphene layers and carbon nanotubes on copper foil. The introduced graphene-CNT hybrid is a remarkable carbon nanostructure with tuneable nano-architectonics that is advantageous for application-oriented design of hierarchical graphene structures. The unique mechanism of synchronized CVD growth of CNT and graphene contributed significantly to the composure of the final carbon structure. Detailed characterization of synthesized pillared graphene shows the cohesive structure and crystalline contact between the two carbon allotropes in the hybrid. Through its tuneable spatial geometry and attractive material properties, this carbon hybrid shows a very promising potential for integration into nanoelectronics, energy storage, and thermal management. These attractive material properties stem from the fact that the synthesized pillared graphene is built from sp^2 hybridized carbon atoms. The direct growth of PGN on copper foil, a significant technical improvement, opens the door for realistic application of PGN that requires mechanically flexible and electrically-thermally conductive substrate. As an immediate proof for the functionality of the refined graphene hybrid structure, it has been readily implemented into a supercapacitor cell. The measurement of the supercapacitor cell demonstrates relatively high energy density with good cycling stability that paves the way for developing future higher energy storage devices.

The presented results in the nanofabrication part of this work are also pioneering for the synchronous approach to synthesis of multi-component hybrids. The introduced fabrication methodology is based on premeditated design of catalysts foundation, analysis of carbon formation mechanisms, and thoughtful timing in the fabrication procedure; as synchronization in the growth process is vital. Accordingly, chemical nature, morphology, and organization of the catalysts, as well as pre-processing of the growth substrate, are the key designing parameters of this method The synchronous parallel CVD growth offers an ideal high-volume technique for carbon hybrids. It also does not involve any unconventional laboratory-style step, and is highly compatible with industrial thin-film fabrication technologies.

In chapter 3 we investigated the potentials of PS-b-PnVP diblock copolymers for developing catalysts arrays and nano-engineering of the pillared graphene architecture. Solvent annealing mechanism allows us to vertically align and control the orientation of cylindrical BCP nano-domains. We managed to successfully align the cylindrical BCP domains, and establish experimental conditions that yield long-range ordering in BCP films. Our results in pattern assisted self-assembly of BCPs have demonstrated a promising route to control bottom-up self-organization processes through top-down designed templates. After successful BCP patterning step, we studied an approach that combines copolymers research with graphene hybrids fabrication. Such development can address the current issues with production and evaluation of graphene based energy devices. It has been shown that the superior nano-patterning capability of block copolymers offers an attractive route to build next generation of pillared graphene nanostructures.

Developing a metrology technique for large-area graphene sheets is a significant requirement for making graphene industry-ready. For utilizing graphene in electronics, displays, and energy devices, an industry-reliable metrology of doped pristine regions, and defect detection are amongst the fundamental needs. The importance of such high-throughput metrology is better understood when we compare it with more conventional techniques for characterizing graphene. While traditional methods such Raman spectroscopy, scanning probe microscopy, and X-ray photoemission spectroscopy can provide valuable information about electronic and structural properties of graphene at an atomic-level, they are often slow and can only cover small regions. Currently, ^{a} large number of graphene experimental studies use only three to five measurements of Raman Spectroscopy (a de facto gold standard in graphene characterization) on selected areas to statistically assess the thickness and quality of a large-scale graphene sheet. This is a high-risk generalization, especially when all parts of the synthesized graphene are to be used for device fabrication. One way to overcome this problem is to obtain Raman maps by scanning the excitation laser point by point over the sample. Considering typical collection time per point (~0.5-1 minute), even with coarse meshing this mapping takes an unrealistically long time for adequate characterization of an industry-scale graphene sheet. For example, mapping a 1cm^2 graphene sheets with a coarse mesh of 1 point per 100μm, requires 10000 measurements and around 150 hours. this is not ideal for the large-area graphene samples produced by CVD or chemical reduction.

In the metrology part of this dissertation we introduced a technique for facile and quick evaluation of processed graphene materials. In particular, we demonstrated the aptitude of fluorescence quenching imaging as a basis for a high-throughput metrology of industrial-scale graphene samples. We exploit fluorescence quenching phenomena and image processing techniques to accurately visualize doped regions in graphene sheets. Our inspiration for this work was the modifications that doping processes cause on the chemical and electronic state of their subject materials. This, in turn, alters the fluorescence quenching condition of doped graphene, compared to that of pristine graphene. Such variation would visually differentiate doped and pristine areas of graphene when it's viewed under a fluorescence microscope. In order to experimentally verify this visualization potential, we first successfully showed the functionality of large-scale FQM in mapping of fluorine-doped regions in graphene sheets. Next, we increased the complexity of the doping pattern and successfully reproduced the mapping results, as a proof to the resolution and scalability strength of our metrology techniques. Upon that, we conducted a comparative investigation on steady-state and time-resolved fluorescence parameters of dye coated graphene, fluorinated graphene, and bare glass as control sample. The fluorometry results support the increasing trend observed in quenching level of DCM dye, from control sample to doped graphene to pristine graphene. Finally we improve our image processing technique by employing Gaussian fitting to determine the contrast regions corresponding to graphene regions. This is a valuable step up since it facilitates the automation of the technique for production-line metrology of graphene.

Thanks to its simplicity, high speed, and small cleanroom footprint (regular confocal microscopy), segmented fluorescence quenching microscopy can be readily adjusted as an in-line graphene measurement technique. Additionally, with proper process automation the method can be integrated with lithography tools, thereby forming the basis of a clustered metrology station.